超高磁場磁気共鳴イメージングによるヒト脳の解剖学的・機能的解析

丸山 修紀

博士 (理学)

総合研究大学院大学
生命科学研究科
生理科学専攻

令和 2 年 (2020) 年度

Anatomical and functional analysis of the human brain with magnetic resonance imaging at ultrahigh fields

Maruyama, Shuki

Doctor of Philosophy

The Graduate University for Advanced Studies, SOKENDAI
School of Life Science
Department of Physiological Sciences

2020

Table of Contents

1. Summary

Magnetic resonance (MR) systems have become one of the most important tools in not only clinical medicine but also brain science researches. Ultrahigh magnetic field (static magnetic field≥7T) strengths can significantly enhance the signal-to-noise-ratio (SNR), contrast-to-noise-ratio (CNR), spatial resolution, and chemical shift dispersion. Thus, it is expected that it will be possible to visualize microstructures of the human brain at a sub-millimeter resolution and high contrast and to observe the subtle changes in the cerebral blood flow and neurometabolites underscoring cognitive function. The goal of my doctoral project was to apply ultrahigh field 7T MR systems to structural and functional brain analysis for advancing the understanding of the higher brain functions of the human brain.

First, I investigated the visualization of the globus pallidus sub-segments in Study I. The success of deep brain stimulation (DBS) targeting the internal globus pallidus (GPi) depends on the accuracy of electrode localization inside the GPi. The GPi, separated from the external globus pallidus (GPe) by the medial medullary lamina (MML), further into the external/internal segment (GPie/GPii) by the accessory medullary lamina (AML). In this study, I sought to compare the visualization of the MML and AML between proton density-weighted (PDW) and T2-weighted (T2W) sequences on 3T and 7T MRI scanners. Eleven healthy participants (five men and six women; age, 19–28 years; mean, 21.5) and one 61-year-old man were scanned using two-dimensional turbo spin-echo PDW and T2W sequences on 3T and 7T MRI scanners with a 32-channel receiver head coil and a single-channel transmission coil. Both qualitative and quantitative evaluation of the visualization of the MML and AML was conducted. Profiles of signal intensity were obtained from the pixel values of straight lines over the GP regions crossing the MML and AML. Contrast ratios (CRs) for GPe/MML, GPie/MML, GPie/AML, and GPii/AML were calculated. Qualitatively, 7T visualized both the MML and AML, whereas 3T visualized the MML less clearly and hardly depicted the AML. Although The signal intensity profiles acquired with PDW and T2W sequences at 3T showed one negative

peak representing the MML. However, the signal intensity profiles acquired with PDW and T2W sequences at 7T showed two negative peaks representing the MML and the AML, distinguishing the GPe, GPie, and GPii. The T2W sequence at 7T yielded significantly higher CRs for GPie/MML, GPie/AML, and GPii/AML than the PDW sequence at 7T or 3T. The T2W sequence at 7T allows visualization of the internal structures of GPi segments with high signal intensity and contrast.

Second, I investigated the primary motor cortex (M1)-centered motor learning network in Study II. M1 is crucial in motor learning. However, it remains unclear how M1 interacts with other brain areas during practice leading to motor learning. Here, I hypothesized that learning-related information is provided by the fronto-parietal execution network (FPN), which is critical for the flexible cognitive control required for practice as a goal-seeking procedure. I combined magnetic resonance spectroscopy (MRS), task fMRI, and resting-state fMRI to depict the sequential finger-tapping learning network. Using a 7T MR machine, I measured GABA and glutamate (Glu) concentration within M1, which regulates network connectivity. A total of 25 participants performed a tapping sequence with their left hand as quickly as possible during fMRI. I conducted MRS and resting-state fMRI before and after the task. MRS was also performed during the task. An increase in the Glu/GABA ratio in the right M1 was positively correlated with task performance improvement. The fronto-parietal regions, including the right M1, demonstrated a learning-related increase in preparatory activity, which overlapped with the FPN and sensorimotor network (SMN). Resting-state fMRI revealed that motor learning-related increments in M1-seeded functional connectivity with the FPN, but not the SMN, were

positively correlated with changes in the Glu/GABA ratio in the M1. These connectivity changes were more prominent in the parietal region than in the frontal region. Our findings indicate that motor learning driven by cognitive control is associated with local variation in the excitatory-inhibitory balance in the M1 that reflects remote connectivity with the FPN, representing the formation of declarative procedural skill.

2. Study I: Comparison of 3T and 7T MRI for the visualization of globus pallidus sub-segments

2.1 Introduction

Deep brain stimulation (DBS) is a stereotactic neurosurgical technique involving the placement of stimulating electrodes to the small subcortical structure (Larson, 2014). DBS targeting the internal region of Globus Pallidus (GPi-DBS) is the treatment of choice for later stages of Parkinson’s disease and medical refractory generalized and segmented dystonia (Koeglsperger et al., 2019). The clinical efficiency of GPi-DBS depends on accurate localization of electrodes inside the GPi (Krack et al., 1998; Tisch et al., 2007; Schönecker et al., 2015).

The GPi is surrounded with the external GP (GPe) and putamen anteriorly, posteriorly, and laterally, the internal capsule (CI), zona incerta (ZI) and medial forebrain bundle (MFB) medially, the nucleus of ansa lenticularis mediodorsally, the optical tract (OPT) ventrally, the amygdala laterodorsally, and the ventral GP laterodorsally (Mai et al., 2015). Electrical current may spread into these regions. Thus the proper placement of the electrode and control of electrical current is critical to prevent side effects (Koeglsperger et al., 2019). More importantly, the stimulation of distinct regions within the GPi causes a different therapeutic outcome. For example, stimulation of the dorsal region of the GPi improves signs and symptoms associated with Parkinson’s disease such as hypokinesia and rigidity. By contrast, although stimulation of the posteroventral region of the GPi reduces hyperkinesia induced by increasing the levodopa dose, it may aggravate gait hypokinesia (Krack et al., 1998; Kumar, 2002; Koeglsperger et al., 2019).

Although the mechanism of the effectiveness of DBS is still incompletely understood, it is supposed to inhibit or excite local neuronal elements (Lozano et al., 2002). There are two theories of improving movement disorders by stimulation: one is based on the function similar to disease (inhibition) (Nambu, 2008); the other is the fact that high-frequency stimulation excites local neuronal elements as local single-pulse stimulation (excitation). This mechanism may include abnormal activity patterns or normalizing neuronal activity pattern (Anderson et al., 2003; Hashimoto et al., 2003; Degos, 2005; Maurice et al., 2013), and inhibition of output nuclei within the basal ganglia circuitry. Nambu (2008) concluded that the mechanism of stimulation of the basal ganglia might abnormal information flow within the circuit in dyskinesia. To further reveal the mechanism of the effective GPi-DBS, detailed anatomical knowledge of the subdivision of the GPi is critical.

The GPi, separated from the GPe by the medial medullary lamina (MML), further into the external/internal segment (GPie/GPii) by the accessory medullary lamina (AML) (Schaltenbrand and Wahren, 1977; Lozano et al., 2002; Zittel et al., 2009; Kita and Jaeger, 2016) (Fig. 1). The localization of the GPi can be visualized pre-operatively from two-dimensional (2D) turbo spin-echo (TSE) proton density-weighted (PDW) or T2-weighted (T2W) images using magnetic resonance imaging (MRI) (Hirabayashi et al., 2002; O'Gorman et al., 2011; Patriat et al., 2018). O'Gorman *et al.* (2011) reported that among various MR imaging sequences [T1-weighted (T1W), T2*-weighted (T2*W), susceptibility-weighted image (SWI), inversion recovery with TSE (IR-TSE), and phase-sensitive IR (PSIR)], the TSE PDW sequence at 1.5T achieves the best visualization of the MML. However, those authors were not always able to visualize the MML. Also, it is difficult to differentiate the GPie and GPii using conventional 1.5T or 3T MRI because the GPi segments are quite small and exhibit low contrast with the AML (Fig. 1).

Recently, ultra-high-field (static magnetic field≥7T) MRI has attracted increasing attention because it can provide higher signal-to-noise-ratio, spatial resolution, and contrast than 1.5T and 3T MRI (Van Der Kolk et al., 2013; Karamat et al., 2016). An increase in the static magnetic field helps visualize microstructures *in vivo* within a reasonable scan time (Thomas et al., 2008; Deistung et al., 2013; Karamat et al., 2016). Accordingly, several attempts have been made to visualize subcortical microstructures, including the GPi, at 7T (Kanowski et al., 2014; Keuken et al., 2014, 2018). One study identified the internal structures of the GPi (GPie, GPii, and AML) in quantitative magnetic susceptibility mapping (QSM) images using 7T MRI (Deistung et al., 2013). However, those authors utilized a method referred to as "calculation of susceptibility through multiple orientation sampling (COSMOS)" (Liu et al., 2009; Wang and Liu, 2015), which took approximately 50 minutes to acquire all gradient (recalled) echo (GRE) data; consequently, this technique is not clinically feasible.

In the present study, I attempted to apply TSE sequences at 7T to obtain ultra-high-resolution images for identifying anatomical substructures of GPi segments within a clinically reasonable scan time. The TSE sequences are less susceptible to inhomogeneity of the static magnetic field than the GRE sequence. By contrast, TSE sequences are associated with several challenges, including inhomogeneity in the transmit magnetic field (B_1 field) and high specific absorption rate (SAR) of the radiofrequency (RF) pulse (Trampel et al., 2011; Balchandani and Naidich, 2015). After optimization of the scan parameters such as input power, flip angle, turbo factor, and repetition time (TR) of TSE sequences within the SAR limitations (Trampel et al., 2011), I visualized the MML and AML using PDW and T2W sequences. The performance of the 7T was compared with 3T images obtained from the same participants.

2.2 Materials and Methods

Participants

This study was approved by the ethical committee of the National Institute for Physiological Sciences, Okazaki, Japan, and was conducted according to the Declaration of Helsinki's guidelines for research involving humans. Written informed consent was obtained from all participants before participation. The participants were eleven healthy volunteers (five men and six women; age, 19–28 years [mean, 21.5]). Also, a 61-year-old man was included in this study. None of the participants had any previous history of neurological or psychiatric disorders.

MR Imaging protocol

All participants were scanned on a 3T MRI scanner (MAGNETOM Verio, Siemens Healthcare, Erlangen, Germany) with a 32-channel receive head coil (Siemens Healthineers, Erlangen, Germany) and a 7T MRI scanner (MAGNETOM 7T, Siemens Healthineers, Erlangen, Germany) with a 32-channel receive head coil and a single-channel transmit coil (Nova Medical Inc., MA, USA). I acquired 2D TSE PDW and T2W images of the whole GP in the axial direction parallel to the anterior commissure-posterior commissure line (AC-PC line) at 3T and 7T. Scan parameters for TSE sequences as follows: TR = 5000 msec; TE = 13 msec for PDW and 53 msec for T2W; matrix size = 448 × 348 at 3T and 432 × 344 at 7T; number of acquisitions (NA) = 2; turbo factor = 7; field of view (FOV) = 224 × 174 mm^2 at 3T and 216 ×

172 mm^2 at 7T; in-plane spatial resolution = 0.5 × 0.5 mm^2; slices = 19; slice thickness = 0.8 mm; bandwidth = 183 Hz/pixel at 3T and 161 Hz/pixel at 7T; acquisition time = 8 minutes 17 sec, and flip angle = 180°. The specific MR imaging parameters are listed in Table 2. The TE of the T2W sequence was optimized with the use of the multi-echo SE sequence and different TEs from 30 msec to 90 msec in 15 msec increments. To visualize the submillimeter microstructure like the MML and the AML, ultra-high-resolution data with 0.5 × 0.5 × 0.8 mm^3 was shown to be necessary. Therefore, I compared the visualization of the MML and the AML using PDW and T2W sequences at the same resolution between 3T and 7T.

At 7T, both T2W and PDW image acquisitions were performed with a prototype TSE sequence, featuring modified RF-pulse shapes for SAR reduction. All scans were performed within the SAR limit of normal operation mode. I acquired transmit magnetic field map to investigate the pads as preliminary experiments. Significant increase in homogeneity was produced by the dielectric pad (Fig. 2). Dielectric pads were placed to the right and left sides of the participant's head while scanning at 7T to improve the uniformity of image intensity resulting from B_1 field inhomogeneity (Teeuwisse et al., 2012a, 2012b). A B_1 map in the center of the brain at the slice containing the GP region was acquired for each participant in order to optimize input power and accurately produce a 90° pulse for TSE sequences. To reduce motion artifacts in the images, which would diminish the visibility of the MML and AML, I collected k-space lines randomly in the segments of the TSE sequences.

Image analysis

For all image analyses, I selected a single slice in which the MML and AML could most easily be identified for right and left GPs. As described above, I acquired all axial images parallel to the AC-PC line at 3T and 7T. Nonetheless, because the slice levels acquired at 3T were not entirely the same as those acquired at 7T, I took a single slice at a similar level for each participant.

Qualitative analysis

All images were viewed on 24-bit gray-scale. The histograms of SI within the GP were obtained, and the histogram metrics such as mean and standard deviation were recorded. The window settings (window width and window level) were adjusted to optimize visibility of the MML and the AML for the bilateral GPs of individual images using the histograms: the window level of the mean pixel value and the window width of ± 3 × standard deviation for 3T-PDW, 3T-T2W, and 7T-PDW images and ± 6 × standard deviation for 7T-T2W images were chosen. I and an experienced MRI researcher (M.F.) evaluated each image for the depiction of the MML and AML based on anatomical information from myelin staining in the atlas of Schaltenbrand and Wahren (Fig. 1) (Schaltenbrand, G. & Wahren, 1977). Whether the MML and AML were visible was assessed by comparison with adjacent and surrounding tissues. The depiction of the MML and AML was determined as “visible” when more than half of them were delineated (Ide et al., 2017). To decrease bias, the two persons resolved all disagreements by consensus reading of images. Particularly the images of an elderly volunteer were separately evaluated and were not included in the qualitative analysis of young volunteers.

Quantitative analysis

Quantitative corrected SI maps were created using Interactive Data Language (IDL, Research Systems Inc., CA, USA) as previously described (De Zwart et al., 2002) with minor modifications. In this study, I used low-resolution calibration data reconstructed from central k-space data for channel sensitivity estimation without additional scan data. The corrected SI of the root-sum-of-squares (RSS) of the combined signals of individual coil images was calculated as follows:

$$Corrected\ SI = \sqrt{S^{H}\Psi^{-1}S} \quad , (1)$$

where S denotes a vector containing the signals from an individual coil, and Ψ denotes the noise correlation matrix, which represents the noise statistics of the coils. Ψ can be calculated as follows:

$$\Psi_{ij} = \sigma \cdot \omega^{2} \cdot \int_{V} A_{i} \cdot A_{j} dr \quad , (2)$$

where σ, ω, A, and V denote conductivity, resonance frequency, magnetic vector potential, and object volume, respectively, and *i, j* denote coil elements.

The average SI profiles were obtained at 0.5-mm intervals from the pixel value of the SI maps on a straight line perpendicular to the maximum diameter of the bilateral GP regions using ImageJ version 1.8.0 (National Institutes of Health, MD, USA; RRID: SCR_003070). The SI profiles were normalized as a function of distance in the GP region using MATLAB R2018a (The MathWorks, Inc., MA, USA; RRID: SCR_001622). I then averaged the SI profiles from each participant. This straight line was drawn manually by me and validated by another MRI researcher (M.F.) to confirm that the line did not include the blood vessels.

In order to quantitatively evaluate the variation of contrast in the GP region, I measured CRs based on the SI maps. For the MML, CRs were calculated between the GPe and MML and between the MML and the GPie. By contrast, for the AML, CRs between the GPie and AML and between the AML and GPii were calculated as follows:

$$CRs = \frac{SI_j}{SI_i} \quad , (3)$$

where i = MML or AML and j = GPe, GPie, or GPii.

I calculated the average SIs in the MML and AML from three points around the negative peaks in the SI profiles, which were considered to correspond to the MML and AML because the thicknesses of the MML and AML are approximately 1 mm in axial slices (Schaltenbrand and Wahren, 1977). I also measured average SIs in the GPe, GPie, and GPii from several points around the corresponding in the profile.

Statistical analysis

All data are expressed as means ± standard deviation. Two-way analysis of variance

(ANOVA) was performed on CRs with factors of the static magnetic field (3T, 7T) and sequence (PDW, T2W). A post-hoc two-sample t-test was performed when significant interaction effects were found. The Bonferroni multiple-comparison correction was performed to adjust the *p*-value. A *p* value less than 0.05 was considered to indicate statistical significance. All analyses were performed using the Statistical Package for the Social Sciences software version 25.0.0 (SPSS, IBM Corp., NY, USA; RRID: SCR_002865).

2.3 Results

Qualitative analysis

Figure 3 shows a comparison of PDW and T2W images taken at 3T and 7T from the same participant. The 7T image visualized both the MML (red arrow) and AML (blue arrow), whereas the 3T image visualized the MML less clearly and hardly depicted the AML as a low SI border within the GP. Specifically, the T2W image at 7T successfully visualized both the MML and AML and achieved high contrast between the GP and surrounding tissues (putamen and internal capsule).

Table 1 summarizes our qualitative analysis of the visibility of the MML and the AML. The 7T image almost entirely visualized both the MML and AML. The visibility of AML was less than 10% at 3T but greater than 90% at 7T.

Quantitative analysis

Figure 4 shows a typical example of the signal intensity (SI) map with a T2W sequence at 7T and profile positions (yellow line). Figure 5A shows a comparison of the SI profiles for the GP region acquired with the PDW sequence at 3T and 7T, and Figure 5B shows a comparison of the SI profiles for the GP region acquired with T2W sequence at both field strengths. The PDW sequence at 7T provided the highest SI. The PDW sequence at 7T exhibited an approximately 2.5-fold increase in SI relative to 3T, whereas the T2W sequence exhibited an approximately 1.6-fold increase. The SI profiles acquired with the PDW and T2W sequences at 3T contain one negative peak, representing the MML (Fig. 5A), whereas those acquired with the PDW and T2W sequences at 7T contain two negative peaks representing the MML and AML, distinguishing the GPe, GPie, and GPii (Fig. 5B).

Figure 6A shows a comparison of contrast ratios (CRs) for the GPe/MML and the GPie/MML. For the GPe/MML, the CRs were 1.11 ± 0.02 for 3T-PDW, 1.09 ± 0.09 for 3T-T2W, 1.12 ± 0.02 for 7T-PDW, and 1.17 ± 0.10 for 7T-T2W, respectively. By contrast, for the GPie/MML, the CRs were 1.08 ± 0.04 for 3T-PDW, 1.07 ± 0.07 for 3T-T2W, 1.06 ± 0.03 for 7T-PDW, and 1.12 ± 0.07 for 7T-T2W, respectively. Although there was a significant main effect of static magnetic field in GPe/MML ($F_{(1, 40)} = 4.644$, $p = 0.037$), no such effect was observed in GPie/MML ($F_{(1, 40)} = 1.529$, $p = 0.223$). No significant main effect of sequence was observed in GPe/MML, and GPie/MML ($F_{(1, 40)} = 0.278$, $p = 0.601$; $F_{(1, 40)} = 2.289$, $p = 0.138$). However, there was an interaction effect between static magnetic field and sequence in GPie/MML ($F_{(1, 40)} = 5.263$, $p = 0.027$). Post-hoc two-sample t-test showed that CRs of 7T-T2W was significantly higher than 3T-T2W and 7T-PDW in GPie/MML ($p = 0.017$ and $p = 0.010$; Bonferroni corrected). No other significant difference in CR was observed in GPe/MML or GPie/MML.

Figure 6B shows a comparison of the CRs for GPie/AML and GPii/AML. For the GPie/AML, the CRs were 1.03 ± 0.04 for 3T-PDW, 1.02 ± 0.07 for 3T-T2W, 1.07 ± 0.02 for 7T-PDW, and 1.15 ± 0.07 for 7T-T2W, respectively. Similar results were shown in GPii/AML; the CRs were 0.98 ± 0.06 for 3T-PDW, 1.02 ± 0.10 for 3T-T2W, 1.03 ± 0.04 for 7T-PDW, and

1.14 ± 0.07 for 7T-T2W, respectively. There were significant main effects of static magnetic field in GPie/AML ($F_{(1, 40)} = 30.680$, $p = 2.099\times10^{-6}$) and GPii/AML ($F_{(1, 40)} = 17.834$, $p = 1.350\times10\text{-}4$). Also, I observed significant main effects of sequence in GPie/AML ($F_{(1, 40)} = 5.292$, $p = 0.027$) and GPii/AML ($F_{(1, 40)} = 14.786$, $p = 4.224\times10^{-4}$). Although the interaction effect between static magnetic field and sequence was significant in GPie/AML ($F_{(1, 40)} = 9.696$, $p = 0.003$), no such effect was observed in GPii/AML ($F_{(1, 40)} = 2.943$, $p = 0.094$). Post-hoc two-sample t-test revealed that the T2W sequence yielded significantly higher CRs in GPie/AML than the PDW sequence at 7T ($p < 0.001$, Bonferroni corrected).

Figure 7 shows a comparison of PDW and T2W images of an elderly volunteer taken at 3T and 7T. The MML and AML were clearly visualized in the PDW and T2W images at 7T. For the elderly participant, similar results were obtained with young volunteers.

2.4 Discussion

In this study, I quantitatively and qualitatively compared the visualization of the MML and AML between PDW and T2W sequences at 3T and 7T. My results demonstrated that PDW and T2W sequences at 7T almost clearly visualized both the MML and the AML. By contrast, in PDW and T2W sequences at 3T, the MML was visualized to some extent, whereas the AML was barely visualized. Also, I showed that the T2W sequence visualized both the MML and AML with significantly higher CRs than the PDW sequence at 7T. To the best of my knowledge, this is the first report to demonstrate that the T2W sequence at 7T allowed the visualization of the internal structures of GPi segments with high SI and contrast.

Technical advantages and challenges of 7T MRI

The therapeutic efficiency of DBS for the treatment of movement disorders depends on the accurate placement of electrodes (Krack et al., 1998; Tisch et al., 2007; Schönecker et al., 2015). Since the anatomical size, position and functional segregation of the GP varies considerably across individuals (Krack et al., 1998; Hirabayashi et al., 2002), it is clinically valuable to use 7T MRI to obtain ultra-high-resolution images that accurately identify the anatomical detail of the target before the operation. In this context, scan time is an important factor. It should be noted that I obtained ultra-high-resolution images of GPi segments using TSE PDW or T2W sequences in only 8 minutes. Although the TSE sequence can provide images without degradation in quality due to inhomogeneity of the static magnetic field, in contrast to the GRE sequence, the TSE sequence has a significant issue of B_1 inhomogeneity at 7T. To solve this problem, I used dielectric pads to improve B_1 inhomogeneity and reduced the required input power. I visually evaluated the effect of various flip angle groups (120°, 140°, 160°, and 180°) on B_1 inhomogeneity in the TSE PDW and T2W images at the slice level of the GP region. However, because I observed little difference in image inhomogeneity among the flip angle groups, I used a flip angle of 180° to obtain higher SI. The TR and turbo factor were adjusted so that all scans could be performed within the SAR limit of normal operating mode.

For DBS targeting, coronal images may also be useful. Nölte *et al.* (2012) have reported that the GPi was more clearly visualized in axial than coronal images using the T2*W sequence. When I applied the MR imaging parameters for axial to coronal scanning, substantial cerebrospinal fluid (CSF) ghost artifacts significantly deteriorated the visualization of the MML and the AML. To minimize the ghost artifacts, synchronizing MRI data acquisition with the cardiac cycle of individual participants is useful (Ide et al., 2014), which requires longer scan time, resulting in the reduction of clinical feasibility. Therefore, in this study, I acquired the axial images from all participants.

Direct comparison with 3T MRI

The MML within GP was completely visualized by, whereas less clearly by 3T (Fig. 3 and Table 1). There was a tendency that 3T-PDW showed higher visibility of the MML and higher CRs in the GPe/MML and GPie/MML than 3T-T2W (Figs. 3, 6A and Table 1), suggesting that the PDW sequence would be superior to the T2W sequence for visualizing the MML at 3T. These findings are consistent with 1.5T results reported previously (O'Gorman et al., 2011) and are explained by the fact that the PDW sequence can provide higher SI reflecting the proton density of tissues since the PDW sequence can minimize the effects of both spin-lattice relaxation time (T1) and spin-spin relaxation time (T2) on the SI in images. Quantitatively, as shown in Figure 6A, there was a main effect of the static magnetic field on the contras ratio (CR) of the GPe/MML, consistent with the qualitative findings. The 7T-PDW shows trends of less CR than 3T-PDW for GPie/MML (Fig. 6A) without statistical significance. Thus it is safe to mention that the PDW sequence of 7T, compared with 3T, provides no improvement in CR. Although I observed no significant difference in CR between 7T-PDW and 7T-T2W in the GPe/MML, I did observe a significant difference in the GPie/MML, indicating that the T2W sequence of 7T has an advantage in visualizing the MML over 3T, leading to better discrimination of GPi from GPe. Since parts of the MML consist of the nerve fibers from the striatum (Nieuwenhuys and Voogd, 1980), the MML has high myelin content (Schaltenbrand and Wahren, 1977; Deistung et al., 2013; Ide et al., 2014, 2017). The 7T-T2W enhances the T2-shortening effects of myelin content in the MML while maintaining a higher SI in the iron-rich GP than 3T.

The AML within the GPi was almost completely visualized by 7T, but not by 3T (Figure 3 and Table 1). The SI profiles at 7T contained discrete negative peaks corresponding to the AML, whereas no such peak was evident in 3T (Fig. 5). As shown in Figure 6B, the main effects of the static magnetic field on the CRs in the GPie/AML and GPii/AML were significant, indicating that 7T provided better contrast of the AML with the surrounding structures (GPie and GPii). The T2W sequence yielded significantly higher CRs in the AML than the PDW sequence at 7T, probably through the same mechanism as MML.

Limitations

The present study has a few limitations. First, my participants were almost young, healthy individuals. Ide *et al*. (2014) reported that there was no significant difference in the visualization of the MML, using QSM and phase difference-enhanced imaging, between ordinary healthy people and patients with Parkinson's disease. Also, they reported that the deposition of iron content in the GP increases with age (Ide et al., 2017). Thus, it is possible that age-related iron deposition in the GP region will affect the visualization of the MML and AML in T2W sequences due to the shortening of the T_2. I additionally acquired the images of an elder participant as a preliminary trial. The visibility of the MML and the AML of an elderly participant was similar to that of young participants between 7T and 3T (Fig. 7), suggesting that 7T will be superior to 3T for identifying the subdivision of GP segments regardless of age. However, due to the limited number of participants, further study will be needed to investigate the magnetic susceptibility effect due to age-related physiological iron/calcium deposition on the visualization of the MML and the AML.

Second, the present study does not precisely demonstrate the improvement of the accuracy of electrode placement within GPi, which will bring better clinical outcomes of GPi-DBS. Further clinical studies are necessary to prove the superior efficacy of 7T over 3T in DBS targeting in the clinical settings, testing the visualization of the internal structures of GP of the elderly population, and the clinical efficacy of DBS targeting guided by the identification of the localization of the AML.

Conclusion

In conclusion, I successfully obtained ultra-high-resolution images for identifying anatomical substructures of GPi segments using PDW and T2W sequences at 7T. Excellent visibility of the AML is useful for differentiating the GPie from the GPii, aiding the orientation for DBS.

2.5 References

Anderson ME, Postupna N, Ruffo M (2003) Effects of high-frequency stimulation in the internal globus pallidus on the activity of thalamic neurons in the awake monkey. J Neurophysiol 89:1150–1160.

Balchandani P, Naidich TP (2015) Ultra-high-field MR neuroimaging. Am J Neuroradiol 36:1204–1215.

De Zwart JA, Ledden PJ, Kellman P, Van Gelderen P, Duyn JH (2002) Design of a SENSE-optimized high-sensitivity MRI receive coil for brain imaging. Magn Reson Med 47:1218–1227.

Degos B (2005) Neuroleptic-Induced Catalepsy: Electrophysiological mechanisms of functional recovery induced by high-frequency stimulation of the subthalamic nucleus. J Neurosci 25:7687–7696.

Deistung A, Schäfer A, Schweser F, Biedermann U, Turner R, Reichenbach JR (2013) Toward in vivo histology: A comparison of quantitative susceptibility mapping (QSM) with magnitude-, phase-, and R2*-imaging at ultra-high magnetic field strength. Neuroimage 65:299–314.

Hashimoto T, Elder CM, Okun MS, Patrick SK, Vitek JL (2003) Stimulation of the subthalamic nucleus changes the firing pattern of pallidal neurons. J Neurosci 23:1916–1923.

Hirabayashi H, Tengvar M, Hariz MI (2002) Stereotactic imaging of the pallidal target. Mov Disord 17:130–134.

Ide S, Kakeda S, Ueda I, Watanabe K, Murakami Y, Moriya J, Ogasawara A, Futatsuya K, Sato T, Ohnari N, Okada K, Matsuyama A, Fujiwara H, Hisaoka M, Tsuji S, Liu T, Wang Y, Korogi Y (2014) Internal structures of the globus pallidus in patients with Parkinson's disease: evaluation with quantitative susceptibility mapping (QSM). Eur Radiol 25:710–718.

Ide S, Kakeda S, Yoneda T, Moriya J, Watanabe K, Ogasawara A, Futatsuya K, Ohnari N, Sato T, Hiai Y, Matsuyama A, Fujiwara H, Hisaoka M, Korogi Y (2017) Internal structures of the globus pallidus in patients with Parkinson's disease: evaluation with phase difference-enhanced imaging. Magn Reson Med Sci 16:304–310.

Kanowski M, Voges J, Buentjen L, Stadler J, Heinze HJ, Tempelmann C (2014) Direct visualization of anatomic subfields within the superior aspect of the human lateral thalamus by MRI at 7T. Am J Neuroradiol 35:1721–1727.

Karamat MI, Darvish-Molla S, Santos-Diaz A (2016) Opportunities and challenges of 7 Tesla magnetic resonance imaging: a review. Crit Rev Biomed Eng 44:73–89.

Keuken MC, Bazin PL, Crown L, Hootsmans J, Laufer A, Müller-Axt C, Sier R, van der Putten EJ, Schäfer A, Turner R, Forstmann BU (2014) Quantifying inter-individual anatomical variability in the subcortex using 7T structural MRI. Neuroimage 94:40–46.

Keuken MC, Isaacs BR, Trampel R, van der Zwaag W, Forstmann BU (2018) Visualizing the human subcortex using ultra-high field magnetic resonance imaging. Brain Topogr 31:513–545.

Kita, H. & Jaeger D (2016) Organization of the Globus Pallidus. In Handbook of basal ganglia and function (Heinz, Steiner. & Kuei YT, ed)., 2nd ed (Elsevier, Amsterdam).

Koeglsperger T, Palleis C, Hell F, Mehrkens JH, Bötzel K (2019) Deep brain stimulation programming for movement disorders: Current concepts and evidence-based strategies. Front Neurol 10:1–20.

Krack P, Pollak P, Limousin P, Hoffmann D, Benazzouz A, Le Bas JF, Koudsie A, Benabid AL (1998) Opposite motor effects of pallidal stimulation in Parkinson's disease. Ann Neurol 43:180–192.

Kumar R (2002) Methods for programming and patient management with deep brain stimulation of the globus pallidus for the treatment of advanced Parkinson's disease and dystonia. Mov Disord 17:198–207.

Larson PS (2014) Deep brain stimulation for movement disorders. Neurotherapeutics 11:465–474.

Liu T, Spincemaille P, De Rochefort L, Kressler B, Wang Y (2009) Calculation of susceptibility through multiple orientation sampling (COSMOS): A method for conditioning the inverse problem from measured magnetic field map to susceptibility source image in MRI. Magn Reson Med 61:196–204.

Lozano AM, Hutchinson WD (2002) Microelectrode recordings in the pallidum. Mov Disord 17:150–154.

Mai J, Majtanik M, Paxinos G (2015) Atlas of the human brain, 4th ed (Academic Press, USA).

Maurice N, Thierry A-M, Glowinski J, Deniau J-M (2013) Spontaneous and evoked activity of substantia nigra pars reticulata neurons during high-frequency stimulation of the subthalamic nucleus. J Neurosci 23:9929–9936.

Nambu A (2008) Seven problems on the basal ganglia. Curr Opin Neurobiol 18:595–604.

Nieuwenhuys, R., Voogd JHC (1988) The human central nervous system (Springer-Verlag, Berlin).

Nölte IS, Gerigk L, Al-Zghloul M, Groden C, Kerl HU (2012) Visualization of the internal globus pallidus: Sequence and orientation for deep brain stimulation using a standard installation protocol at 3.0 Tesla. Acta Neurochir (Wien) 154:481–494.

O’Gorman RL, Shmueli K, Ashkan K, Samuel M, Lythgoe DJ, Shahidiani A, Wastling SJ, Footman M, Selway RP, Jarosz J (2011) Optimal MRI methods for direct stereotactic targeting of the subthalamic nucleus and globus pallidus. Eur Radiol 21:130–136.

Patriat R, Cooper SE, Duchin Y, Niederer J, Lenglet C, Aman J, Park MC, Vitek JL, Harel N (2018) Individualized tractography-based parcellation of the globus pallidus pars interna using 7T MRI in movement disorder patients prior to DBS surgery. Neuroimage 178:198–209.

Schaltenbrand, G. & Wahren W (1977) Atlas for stereotaxy of the human brain (Thieme, Stuttgart).

Schönecker T, Gruber D, Kivi A, Müller B, Lobsien E, Schneider GH, Kühn AA, Hoffmann KT, Kupsch AR (2015) Postoperative MRI localisation of electrodes and clinical efficacy of pallidal deep brain stimulation in cervical dystonia. J Neurol Neurosurg Psychiatry 86:833–839.

Teeuwisse WM, Brink WM, Haines KN, Webb AG (2012a) Simulations of high permittivity materials for 7T neuroimaging and evaluation of a new barium titanate-based dielectric. Magn Reson Med 67:912–918.

Teeuwisse WM, Brink WM, Webb AG (2012b) Quantitative assessment of the effects of high-permittivity pads in 7 tesla MRI of the brain. Magn Reson Med 67:1285–1293.

Thomas BP, Welch EB, Niederhauser BD, Whetsell WO, Anderson AW, Gore JC, Avison MJ, Creasy JL (2008) High-resolution 7T MRI of the human hippocampus in vivo. J Magn Reson Imaging 28:1266–1272.

Tisch S, Zrinzo L, Limousin P, Bhatia KP, Quinn N, Ashkan K, Hariz M (2007) Effect of electrode contact location on clinical efficacy of pallidal deep brain stimulation in primary generalised dystonia. J Neurol Neurosurg Psychiatry 78:1314–1319.

Trampel R, Ott DVM, Turner R (2011) Do the congenitally blind have a stria of gennari? first intracortical insights in vivo. Cereb Cortex 21:2075–2081.

Van Der Kolk AG, Hendrikse J, Zwanenburg JJM, Visser F, Luijten PR (2013) Clinical applications of 7 T MRI in the brain. Eur J Radiol 82:708–718

Wang Y, Liu T (2015) Quantitative susceptibility mapping (QSM): Decoding MRI data for a tissue magnetic biomarker. Magn Reson Med 73:82–101.

2.6 Figure Legends

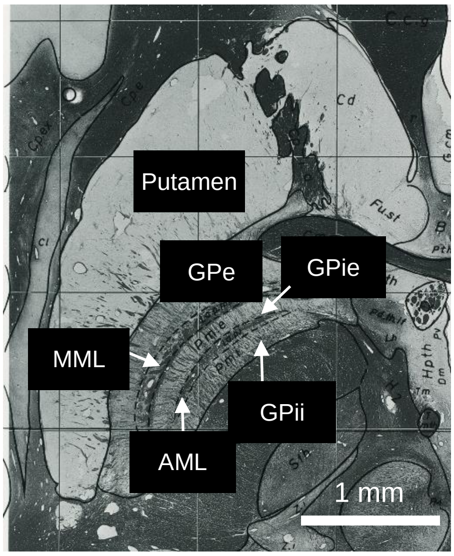

Fig. 1. Myelin stain at the level of the GPi (plate 54) from the Schaltenbrand and Wahren atlas for stereotaxy of the human brain (Schaltenbrand, G. & Wahren, 1977).

The images are not covered by the CC BY license. All rights reserved, used with permission from Georg Thieme Verlag KG, Germany.

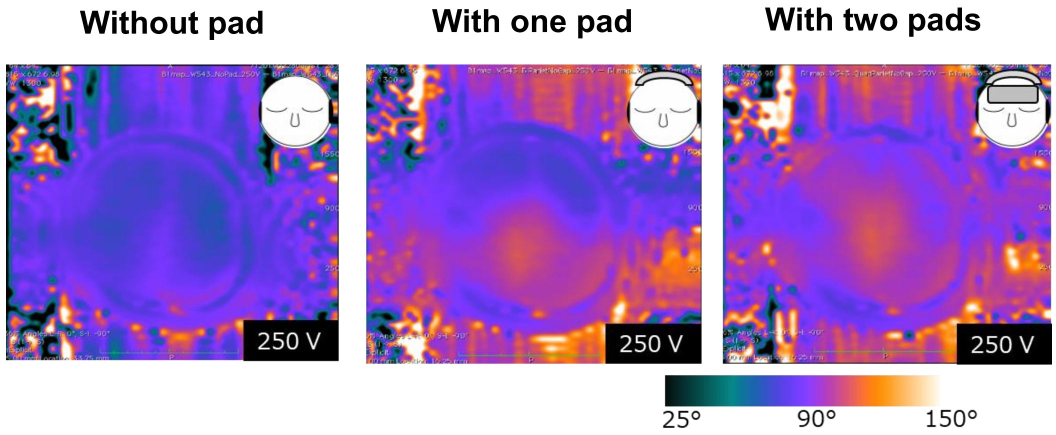

Fig. 2. Transmit magnetic field map of the participant at 7T when the transmit input power was 250 V.

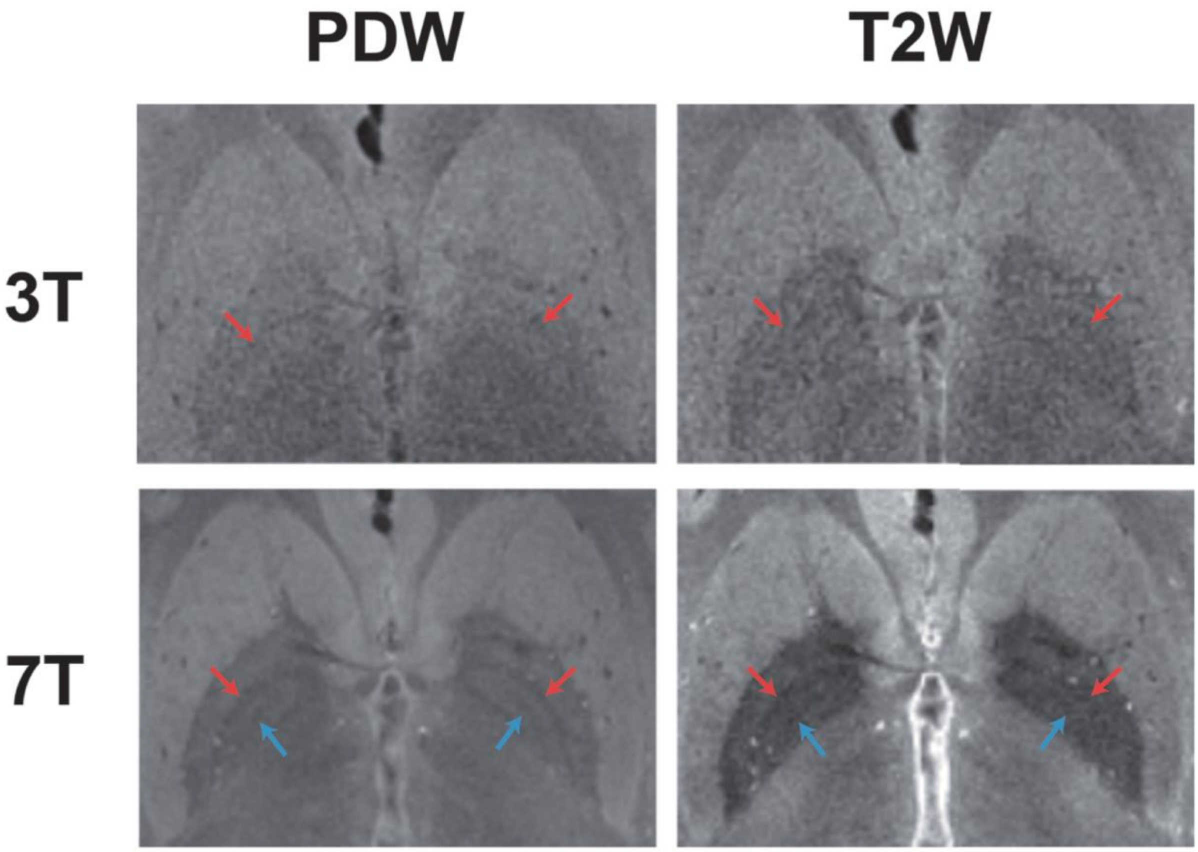

Fig. 3. Comparison of the PDW and T2W images of the same participant at 3T and 7T. 7T visualized both the MML (red arrow) and AML (blue arrow), whereas 3T visualized the MML less clearly and hardly depicted the AML.

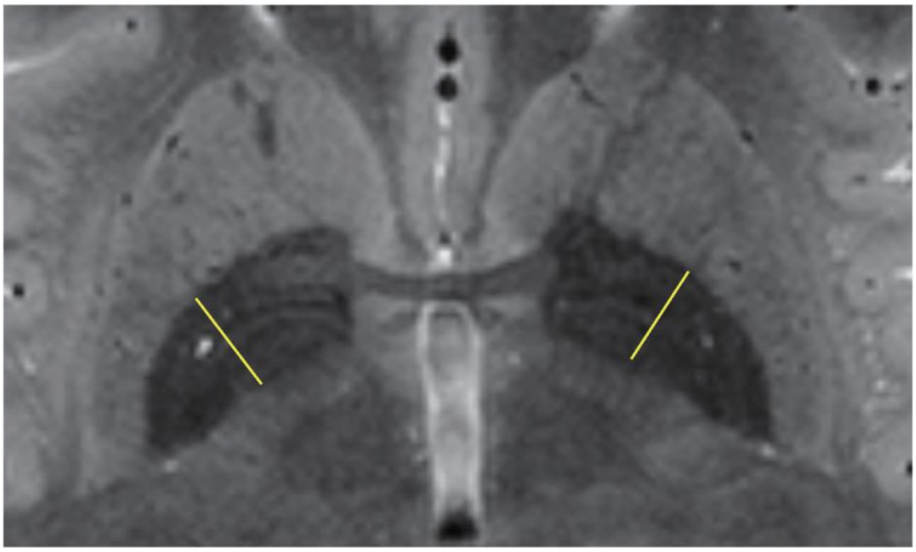

Fig. 4. A typical example of an SI map acquired with the T2W sequence at 7T, with typical profile positions (yellow line).

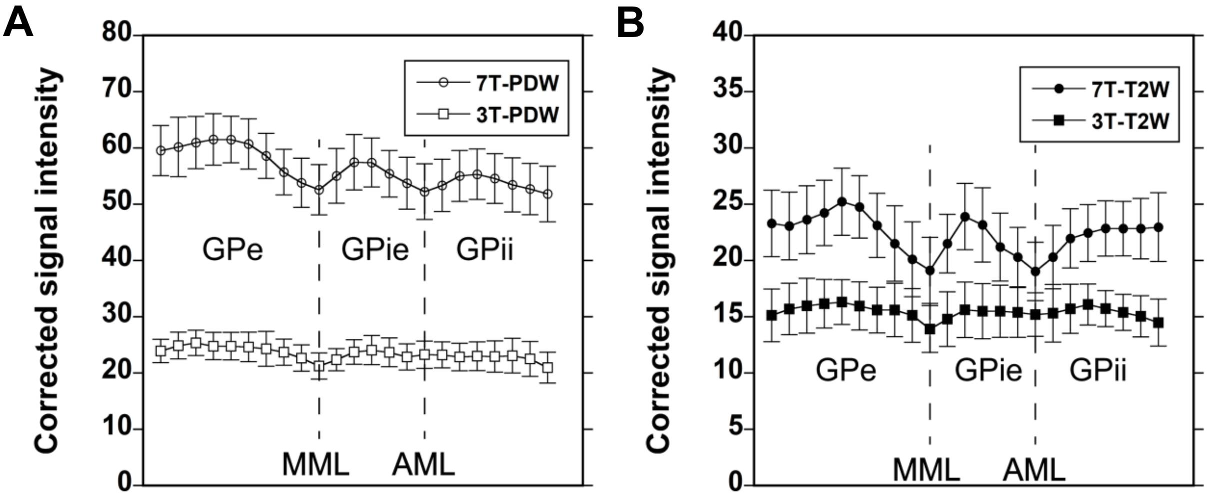

Fig. 5. Comparison of SI profiles for the GP region acquired with the PDW (a) and T2W (b) sequences at 3T and 7T.

Data are means ± standard deviation (n = 11).

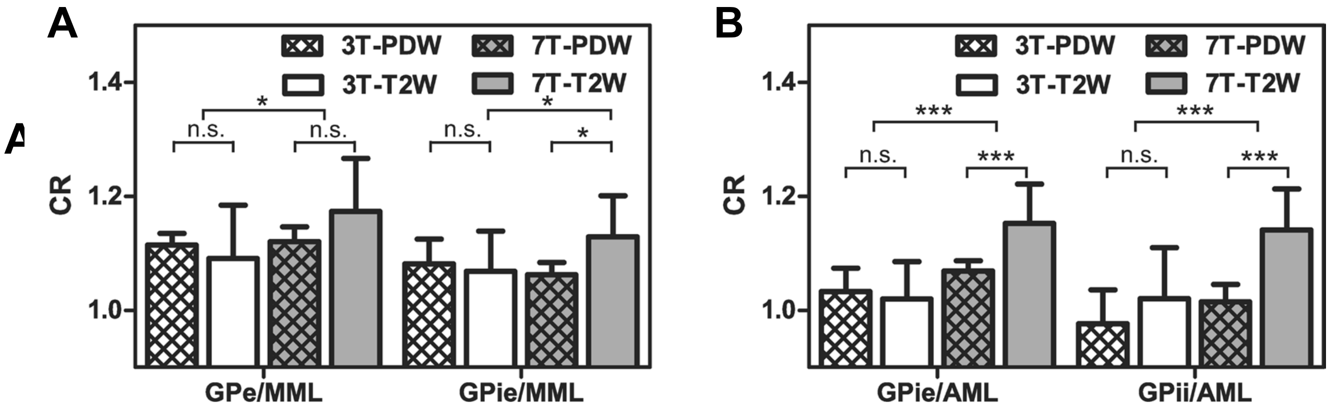

Fig. 6. Comparison of CRs for GPe/MML, GPie/MML, GPie/AML, and GPii/AML.

Data are means ± standard deviation (n = 11). Asterisks indicate the significance level of two-way ANOVA and post-hoc two-sample t-test (***$p < 0.001$, *$p < 0.05$).

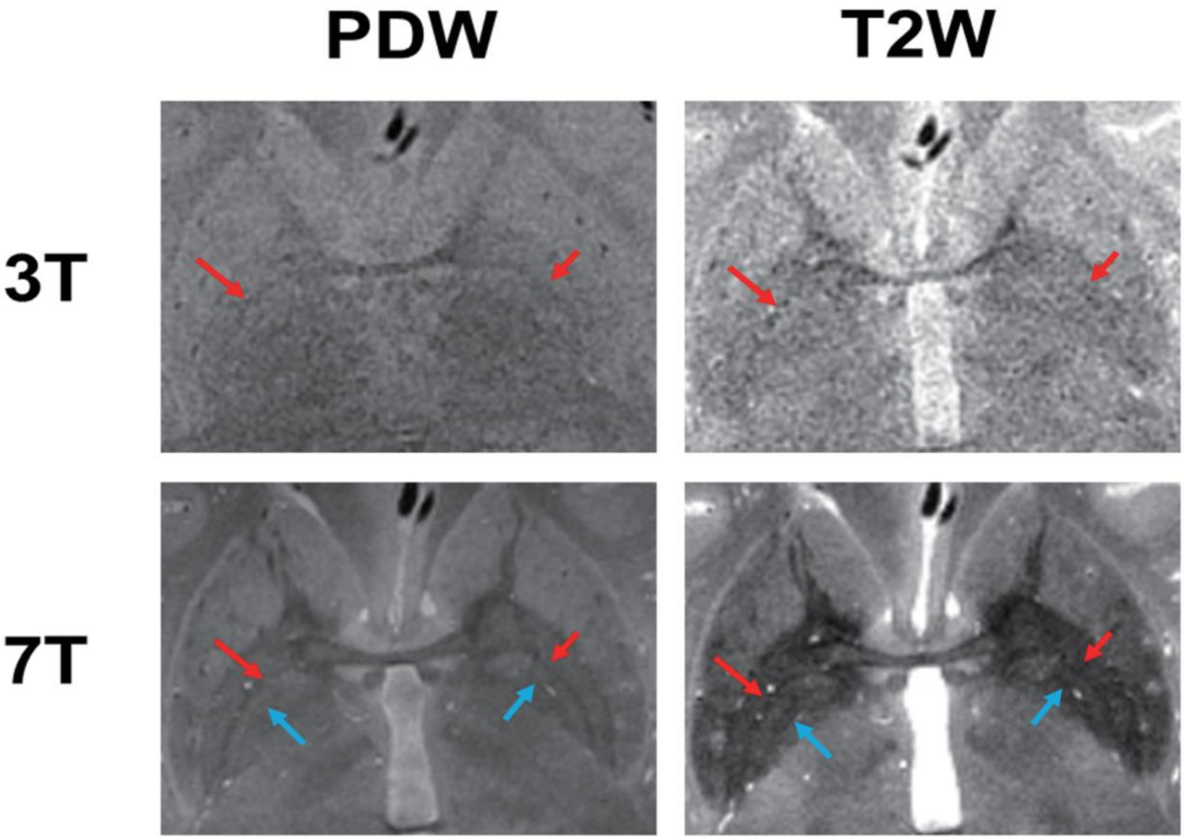

Fig. 7. Comparison of the PDW and T2W images of the elderly participant at 3T and 7T. 7T visualized both the MML (red arrow) and AML (blue arrow), whereas 3T visualized the MML less clearly and hardly depicted the AML.

2.7 Tables

Table 1. Qualitative analysis of the visibility of the MML and AML.

		MML		AML	
		Left	Right	Left	Right
7T	PDW	10 (90.9%)	11 (100%)	10 (90.9%)	10 (90.9%)
	T2W	11 (100%)	10 (90.9%)	10 (90.9%)	10 (90.9%)
3T	PDW	5 (45.5%)	8 (72.7%)	1 (9.1%)	1 (9.1%)
	T2W	4 (36.4%)	4 (36.4%)	0 (0%)	1 (9.1%)

Table 2. MR Imaging parameters

	FOV	Matrix	Resolution	Slices	TR	TE	Bandwidth	NA	Acquisition time
3T	224 × 174 (mm^2)	448 × 348	0.5 × 0.5 × 0.8 (mm^3)	19	5000 msec	13 msec (PDW) 53 msec (T2W)	183 (Hz/Pixel)	2	8 min 17 sec
7T	216 × 172 (mm^2)	432 × 344					161 (Hz/Pixel)		

3. Study II: Sequential finger-tapping learning mediated by the primary motor cortex and fronto-parietal network: A combined MRI-MRS study

3.1 Introduction

Motor learning refers to the acquisition of new spatiotemporal muscle activation patterns (Sanes and Donoghue, 2000). Practice is a critical factor for motor learning, which is characterized by a goal-seeking process with a feedback, leading to a configurational change in movement in terms of speed and accuracy (Shmuelof et al., 2012), representing the performer's attempt to reach a goal (Miller et al., 1960; Guadagnoli and Lee, 2004). Thus, practice requires externally directed attention toward a goal and feedback, and internally directed attention toward the motor control. The difference between a goal and feedback is referred to as challenge, which is crucial for motor skill learning and retention (Guadagnoli and Lee, 2004; Wadden et al., 2019). Challenge makes trainees exert an effort into the relevant training; for example, the sequential finger-tapping learning paradigm is frequently utilized in the neuroimaging field (Fischer et al., 2002, 2005; Walker et al., 2002, 2003; Debas et al., 2010; Hamano et al., 2020). In studies using this paradigm, participants are usually instructed to practice a given sequence "as fast and as accurately as possible." In these situations, participants must first retrieve the sequence to conduct the practice. Speed pressure enhances the learning process because the instruction of "as fast as possible" maintains the difference between the goal and performed output; thus, the task remains challenging. This type of practice for motor learning requires flexible cognitive control (Marek and Dosenbach, 2018) of externally and internally directed attention, in addition to the motor control.

The primary motor cortex (M1) plays an essential role in motor skill learning (Sanes and Donoghue, 2000; Dayan and Cohen, 2011; Shmuelof and Krakauer, 2011; Dupont-Hadwen et al., 2019). M1 comprises the intrinsic horizontal connection network necessary to support learning-induced reorganization (Sanes and Donoghue, 2000) dependent on the precise balance of excitatory and inhibitory signaling within the system. Control at the local inhibitory level is critical to enable the functional restructuring of intracortical connections, leading to a change in the M1 output map (Sanes and Donoghue, 2000). The modulation of inhibitory GABA levels in M1, measured using magnetic resonance spectroscopy (MRS), by anodal transcranial direct current stimulation enhances motor learning (Stagg et al., 2011a). Kolasinski et al. (2019) reported a dynamic reduction of GABA levels within M1 during motor skill learning using a serial reaction time task and MRS. Combining MRS and resting-state fMRI has permitted an exploration of the relationship between learning-related changes in the resting-state network and the formation of motor engrams in M1. A learning-related reduction in GABA levels in M1 correlated with functional connectivity strength changes in the resting-state sensorimotor network (SMN) in long-term motor learning (Sampaio-Baptista et al., 2015). Baseline GABA levels in M1 are positively correlated with motor learning-related changes in resting-state functional connectivity between the bilateral M1s and between the right M1 and left superior parietal cortex (King et al., 2020). These studies evaluated the relationship between GABA levels of the M1 and network changes in motor task-relevant regions.

Meanwhile, as a goal-seeking behavior, practice for motor learning requires executive control, suggesting involvement of the fronto-parietal execution network (FPN) (Vincent et al., 2008). Herein, we hypothesized that learning-related information during goal-seeking practice is provided by the FPN, in addition to the SMN (Chenji et al., 2016). We measured the levels of glutamate (Glu) and GABA in the M1, as these neurotransmitters play an essential role in the neural circuits underpinning learning and memory (Steele and Mauk, 1999; Riedel et al., 2003). We combined MRS, task fMRI, and resting-state fMRI to depict the network level changes during sequential finger-tapping learning with the non-dominant left hand, under speed-pressure, using a 7T MR machine. This study aimed to depict the M1-centered network for motor learning through goal-seeking practice. To control the learning effect non-specific to the sequence, another group of thirteen participants underwent the identical procedure except that they tapped 120 different sequences.

3.2 Materials and Methods

Participants

A total of 43 healthy, right-handed adult volunteers participated in the study (3 males and 36 females: mean age (± SD) was 22.9 ± 4.4 years). Handedness was assessed using the Edinburgh Handedness Inventory (Oldfield, 1971). None of the participants had a history of neurological or psychiatric diseases. All participants provided written informed consent for participation in the experiment. The study was conducted according to the Declaration of Helsinki and was approved by the Ethical Committee of the National Institute for Physiological Sciences, Japan.

Experimental design

We performed MRS-fMRI experiments using a 7T MRI scanner (MAGNETOM 7T, Siemens Healthineers, Erlangen, Germany) with a 32-channel receiving head coil and a single-channel transmitting coil (Nova Medical Inc., MA, USA). All participants underwent resting-state fMRI and MRS scans before and after the motor sequence learning tasks, as well as one MRS and four fMRI scans during motor sequence learning tasks in the task session (Fig. 1A). Dielectric pads (CaTiO3) (Webb, 2011) were placed around each participant's head while scanning at 7T to improve the B1 transmit field inhomogeneity (Teeuwisse et al., 2012a, 2012b). All scans were performed within the Specific Absorption Rate (SAR) limit of the normal operation mode.

Motor sequence learning task

Thirty participants were asked to perform pre-determined five-digit sequences "4-1-3-2-4" (n = 17) or "2-3-1-4-2" (n = 13) as quickly and accurately as possible, in the MRI scanner (Fig. 1B) (Walker et al., 2002, 2003; Hamano et al., 2020). Additionally, thirteen participants were asked to perform 120 different sequences to assess the non-specific learning as control condition. The sequence "4-1-3-2-4" corresponds to "index-little-middle-ring-index." The motor sequence task consisted of six 30-s tapping epochs followed by 30-s rest epochs that were repeated five times (Fig. 1B). The visual feedback signals were displayed using a projector (Optoma EH503; Optoma Inc., Fremont, CA, USA) with a lens (APO 50-500 mm F4.5-6.3 DG OS HSM; SIGMA, Kanagawa, Japan) on a screen viewed by the participants via a mirror mounted to the receiving head coil. Response time was measured using Presentation software version 16.4 (Neurobehavioral Systems, NY, USA; RRID: SCR_002521). The rest epoch started with the appearance of the instruction "Rest" on the screen for 500 ms, followed by a 500-ms presentation of four blue circles aligned within an equally spaced horizontal array. The instruction "Task" appeared for 2 s at the end of the rest epoch as a signal to the participants to retrieve motor sequences and prepare for their execution (Fig. 1B). The task epoch started with four closed white circles presented for 500 ms, which changed into open circles. During the task epoch, participants tapped the button box (Current Design, Philadelphia, USA) according to the sequence shown at the top of the screen (i.e., "4-1-3-2-4"). Visual feedback of correct tapping was provided by filling the white circle corresponding to the tapped finger. When the participant provided an incorrect response, the visual feedback signal remained at the previous position until the correct button was tapped. Task performance was measured using transition time (TT), defined as the average time between two correct button responses per epoch. The performance improvement was calculated using the following equation:

$$Performance\ \ improvement\ \ (\%) = \frac{(TT_1 - TT_5)}{TT_5} \times 100 \qquad ,(1)$$

where TT_1 indicates the transition time at block 1 and TT_5 indicates the transition time at block 5.

The task performance data were analyzed using repeated-measures analysis of variances (ANOVA), with block as a factor, performed using the Statistical Package for the Social Sciences software version 25.0.0 (SPSS, IBM Corp., NY, USA; RRID: SCR_002865). Two participants were excluded due to a statistical outlier in the TT values (> 2 SD).

Structural data acquisition

Three dimensional T1-weighted (T1w) images were acquired for anatomical reference (Magnetization Prepared Rapid Acquisition Gradient Echo [MPRAGE] (Mugler and Brookeman, 1990), TR/TE = 3,000/3.08 ms; inversion time [TI] = 1,200 ms; field of view = 240×225 mm^2; matrix size = 320×320; slice thickness = 0.75 mm; 224 slices; generalized auto-calibrating partially parallel acquisitions [GRAPPA] (Griswold et al., 2002) acceleration factor = 3; bandwidth = 230 Hz/Px; flip angle = 14°; acquisition time = 4 min 50 s).

fMRI data acquisition

fMRI images were acquired before, during, and after the motor sequence learning tasks using a multiband gradient-echo echo-planar imaging sequence (Moeller et al., 2010). The scan parameters were set as per the human connectome project (HCP) 7T protocol (Vu et al., 2017) (TR/TE = 1,000/22.2 ms; field of view = 208×208 mm^2; matrix size = 130×130; slice thickness = 1.6 mm; 85 slices; multi-band/GRAPPA acceleration factor = 5/2; bandwidth = 1,924 Hz/Px; flip angle = 45°). The spin echo field map was acquired (Andersson et al., 2003) (TR/TE = 3,000/60 ms; field of view = 208×208 mm^2; matrix size = 130×130; slice thickness = 1.6 mm; 85 slices; multi-band/GRAPPA acceleration factor = 5/2; bandwidth = 1,924 Hz/Px; flip angle = 180°; acquisition time = 1 min 26 s). A B1 transmit field map in the center of the brain, around the slice of the M1 hand knob area, was acquired for each participant to optimize the input power for accurately producing a 90° pulse for all fMRI scans. In particular, participants were instructed to keep their eyes open while viewing a fixation cross, and to avoid specific thoughts or falling asleep during resting-state fMRI scans.

MRS data acquisition

A 2×2×2 cm^3 volume of interest was centered over the right M1 hand knob area (Fig. 2A), without dura, on T1w MPRAGE images. The hand knob area was identified using fMRI during a sequential finger opposition task with the left hand (TR/TE = 1,000/24 ms; field of view = 192×192 mm^2; matrix = 96×96; slice thickness = 2 mm; 20 slices; GRAPPA acceleration factor = 2; bandwidth = 2,170 Hz/Px; flip angle = 45°; acquisition time = 3 min 30 s). Ultra-short TE MRS data were acquired before, during, and after the motor sequence learning task using the STimulated Echo Acquisition Mode (STEAM) sequence (TR/TE = 5,000/5.68 ms; mixing time = 40 ms; vector size = 2,048; bandwidth = 4,000 Hz/Px; average = 64) with VAriable Power RF pulses with Optimized Relaxation delays (VAPOR) water suppression (Tkáč et al., 1999, 2009). The STEAM sequence was combined with outer volume suppression to improve localization performance. A 4-average water reference signal was acquired for eddy current correction (Klose, 1990) and absolute quantification of the metabolites. Before data acquisition, all first- and second-order shim terms were automatically adjusted with the fast automatic shim technique using echo-planar signal readout for mapping along with projections (FASTMAP) (Gruetter, 1993; Gruetter and Tkáč, 2000). In addition, B1 transmit field strength for localization pulses and VAPOR water suppression were adjusted for individual participants.

HCP-style structural data acquisition with 3T MRI and preprocessing

In addition to the MRS-fMRI data acquisition using 7T MRI, the HCP-style structural data of all participants were obtained using a 3T MRI scanner (Magnetom Verio, Siemens Healthcare, Erlangen, Germany) with a 32-channel receiving head coil (Siemens Healthcare, Erlangen, Germany). The obtained 3T MRI data were utilized to correct the geometric distortion of the 7T MR data (Yamamoto et al., 2020, see below, *fMRI preprocessing*). Scan parameters were as per the HCP 3T protocol with minor modifications (Glasser et al., 2013). Three-dimensional T1w images were acquired (MPRAGE (Mugler and Brookeman, 1990), TR/TI/TE = 2,400/1,060/2.24 ms; field of view = 256×240 mm^2; matrix size = 320×320; slice thickness = 0.8 mm; 224 slices; GRAPPA acceleration factor = 2; bandwidth = 210 Hz/Px; flip angle = 8°; acquisition time = 6 min 38 s; measurement = 2). Three-dimensional T2 weighted (T2w) images were acquired (Sampling Perfection with Application optimized Contrast using different angle Evolutions [SPACE] (Mugler, 2014), TR/TE = 3,200/560 ms; field of view = 256×240 mm^2; matrix size = 320×320; slice thickness = 0.8 mm; 224 slices; GRAPPA acceleration factor = 2; bandwidth = 744 Hz/Px; turbo factor = 167; acquisition time = 6 min; measurement = 2). All data were processed using the structural pipeline (PreFreeSurfer, FreeSurfer, and PostFreeSurfer) of the minimal HCP preprocessing pipeline version 4.0.0-alpha.5, including the following steps: gradient magnetic field nonlinearity distortion correction, T2w images to T1w image registration, and Montreal Neurologic Institute (MNI) volume registration (Glasser et al., 2013).

MRS data analysis

Raw MRS data were post-processed using MATLAB R2018a (The MathWorks, Inc., MA, USA; RRID: SCR_001622). Motion-corrupted data were removed to improve the spectral quality (Simpson et al., 2017). To quantify the proportion of gray matter (GM), white matter (WM), and cerebrospinal fluid (CSF) fractions in the volume of interest, segmentation in SPM was applied to the T1w MPRAGE images. Eddy current correction and frequency correction were performed using a water reference scan, and the zero and first-order phases of the array coil were aligned using the cross-correlation method of MRspa (RRID: SCR_017292). Subsequently, LCModel version 6.3-1N (Stephen Provencher, Inc., ON, Canada; Provencher, 1993, 2001; RRID: SCR_014455) analysis was used to quantify the concentration of neurochemicals within the chemical shift range of 0.5 to 4.1 ppm (Provencher, 2001). Other parameters in the LCModel were as reported previously (Marjańska and Terpstra, 2019). The concentrations of GABA and Glu were normalized to that of total creatine (tCr). The change in glutamate to GABA ratio (Glu/GABA) after the motor sequence learning task was calculated using the following equation:

$$\mathrm{Glu/GABA\,change}\ \ (\%) = \frac{\left(\mathrm{Glu/GABA}_{post} - \mathrm{Glu/GABA}_{pre}\right)}{\mathrm{Glu/GABA}_{pre}} \times 100 \qquad , (2)$$

where $\mathrm{Glu/GABA}_{\mathrm{pre}}$ and $\mathrm{Glu/GABA}_{\mathrm{post}}$ indicate the Glu/GABA ratio at pre-task and post-task, respectively. The distribution of GABA and Glu concentrations was visualized using the RainCloudPlots Python-script (Allen et al., 2019; https://github.com/RainCloudPlots/RainCloudPlots).

Repeated-measures ANOVA was performed using SPSS, with the concentrations of GABA and Glu at different time points (pre-task, during-task, and post-task) as a factor. The Cramer–Rao lower bounds (CRLB) and water linewidth at FWHM were used for the quality control of spectra (Provencher, 2001). The CRLB was calculated using LCModel, and water linewidth was obtained by fitting to the additional water spectrum using MATLAB. Data were excluded when CRLB > 15 % (n = 1), linewidth > 19 Hz (n = 1). Repeated-measures ANOVA was performed on the CRLB and water linewidth time points (pre-task, during-task, and post-task) with a within-subjects factor using SPSS.

fMRI preprocessing

All fMRI data were processed using the functional pipeline (fMRIVolume) of the minimal HCP preprocessing pipeline (Yamamoto et al., 2020). This pipeline included the following steps: motion correction, gradient magnetic field nonlinearity distortion correction, field map-based distortion correction (Topup) (Andersson et al., 2003), nonlinear registration into 3T MNI structure data, and grand-mean intensity normalization. Finally, volume-based smoothing with a 5-mm full width at half maximum (FWHM) Gaussian kernel was applied.

Task fMRI data analysis

Task fMRI data analysis was performed using Statistical Parametric Mapping (SPM12; RRID: SCR_007037) in MATLAB R2018a. A general linear model (GLM) was fitted to the fMRI data for each participant (Friston et al., 1994; Worsley and Friston, 1995). The fMRI time series for preparation phases 2 s before task execution and execution phases were modeled with boxcar functions convolved with the canonical hemodynamic response function. Each block comprised six execution-related and preparation-related regressors. The design orthogonality between the execution and preparation phases was −0.0137 ± 0.054 for block 1, −0.0141 ± 0.054 for block 2, −0.0137 ± 0.054 for block 3, and −0.0139 ± 0.054 for block 4 (mean ± SD). A temporal high-pass filtering with a cutoff frequency of 1/128 Hz was applied. Using a first-order autoregressive model, the serial autocorrelation was estimated from the pooled active voxels with the restricted maximum likelihood procedure, and subsequently used to whiten the data (Friston et al., 2002). Several nuisance covariates, including six head motion parameters and CSF time-series, were incorporated into the model. The parameter estimates for each execution-related and preparation-related regressors were evaluated using constant and predefined linear contrasts. Increasing contrast vectors were defined numerically as an increment of one per block, keeping the mean equal to zero.

For group-level analysis of task fMRI data, one-sample t-tests of participants' contrast images were performed (Holmes and Friston, 1998). The resulting set of voxel values for each contrast constituted the SPM{t}. We calculated the T-score of linear increment in preparation-related activity in right M1 in non-specific learning. The statistical threshold was set at $p < 0.05$, FWE-corrected at the voxel-level (Friston et al., 1996), unless otherwise specified.

Anatomical labeling and visualization

MRIcron (RRID: SCR_008264) was used to display fMRI activation maps on a standard brain image. The Automated Anatomical Labeling atlas was used for anatomical labeling (Tzourio-Mazoyer et al., 2002).

Resting-state fMRI data analysis

Resting-state functional connectivity analysis was conducted using the CONN toolbox version 17 in SPM12 (Whitfield-Gabrieli and Nieto-Castanon, 2012; RRID:SCR_009550). An anatomical component-based noise correction method (aCompCor) (Behzadi et al., 2007) was applied to remove the five components of signals from WM, CSF, and residual head motion-related signals through linear regression. A temporal bandpass filtering of 0.008–0.090 Hz was applied.

Seed-to-voxel correlation analysis was performed at the individual level. We selected the preparation-related increased voxels in M1 (MNI: x = 36, y = −25, z = 51), determined in the second-level analysis of task fMRI (FWE voxel-level corrected $p < 0.05$), as a seed region of interest (ROI) (Fig. 6A). An individual seed-based functional connectivity map was obtained by computing Pearson’s correlation coefficients between the time-series from the M1 seed ROI and the time-series of all other voxels across the whole brain. Fisher’s r-to-*z* transformation was used to convert the correlation coefficients into *z*-scores. M1-seeded functional connectivity changes were integrated using the following equation using AFNI version 18.1.32. (Cox, 1996; RRID: SCR_005927):

$$Connectivity\ change\ = \sum\left(Connectivity_{post} - Connectivity_{pre}\right)\ , (3)$$

where $\text{Connectivity}_{pre}$ and $\text{Connectivity}_{post}$ are the pre-task and post-task functional connectivity values, respectively.

We calculated the changes in functional connectivity within ROIs of the SMN and FPN defined from CONN's ICA analyses of the HCP dataset of 497 individuals. The SMN includes the supplementary motor cortex and bilateral sensorimotor cortex, whereas the FPN consists of the bilateral lateral prefrontal cortex (LPFC) and posterior parietal cortex (PPC). The correlations between Glu/GABA changes within M1 and M1 seed-based functional connectivity changes were analyzed using linear regression analysis.

3.3 Results

MRS spectra

Figure 2A shows an example of MR spectra within M1 obtained using the 7T MR system. The 2×2×2 cm^3 volume of interest was centered over the hand knob area of the right M1 identified using fMRI during a finger opposition task (red), and was superimposed on T1w MPRAGE images. To investigate whether the changes in metabolite concentrations were due to fluctuations in spectral quality, we evaluated the Cramer–Rao lower bounds (CRLB) and linewidth. MRS spectra provided reliable estimates of multiple metabolites with a CRLB < 15%. Repeated-measures ANOVA revealed no significant main effect of time (pre-task vs. during-task vs. post-task) on CRLB and linewidth (Table 1).

Figure 2B shows the distribution of the concentrations of GABA/tCr and Glu/tCr in the pre-, during-, and post-task periods. The variation in neurotransmitter concentration was analyzed using repeated-measures ANOVA with time as a factor (pre-task vs. during-task vs. post-task). No significant change in GABA/tCr concentration ($F_{(2,48)} = 0.114$; $p = 0.893$) was observed. A significant main effect of time on Glu/tCr concentration ($F_{(2,48)} = 11.857$; $p = 6.536\times10^{-5}$ was noted. Post-hoc one-sample t-tests revealed significant reductions in the Glu/tCr concentration between the pre- and post-task periods ($p = 1.860\times10^{-4}$ with Bonferroni correction) and between during- and post-task periods ($p = 0.040$ with Bonferroni correction).

Task performance

Task performance was evaluated using transition time of the consecutive finger tapping (Fig. 3A). The transition times were 258.063 ± 46.213 for block 1, 202.490 ± 31.049 for block 2, 184.320 ± 26.285 for block 3, 178.237 ± 22.600 for block 4, and 173.673 ± 19.417 for block 5 (mean ± SD). Repeated-measures ANOVA revealed a significant main effect of time (blocks 1–5) ($F_{(4,96)} = 124.035$; $p = 4.872 \times 10^{-37}$). Post-hoc one-sample t-tests revealed that the transition time did not significantly differ between blocks 4 and 5 ($p = 0.389$ with Bonferroni correction), indicating that performance plateaued. The relationship between the change in Glu/GABA ratio within M1 and performance improvement was evaluated using linear regression analysis. A positive correlation was observed between the change in the Glu/GABA ratio and performance improvement ($r_{(25)} = 0.42$, $p = 0.038$) (Fig. 3B).

Execution-related and preparation-related activity

Task fMRI showed the task execution-related activity in the bilateral M1, cerebellum (CB) lobules, supplementary motor area (SMA), thalamus (Thal), superior parietal lobule (SPL), and right primary somatosensory cortex (S1) (FWE-corrected $p < 0.05$ at voxel-level) (Fig. 4A). Preparation-related activity was observed in the bilateral putamen (Put), insula, M1, SMA, Thal, SPL, middle occipital lobe (MOL), right primary somatosensory cortex (S1), and middle frontal gyrus (MFG) (FWE-corrected $p < 0.05$ at peak level; Fig. 4B).

Linear increments in execution-related and preparation-related activity

We observed linear increments in execution-related activity in the right M1, S1, and inferior occipital lobe (IOL) with lenient threshold (uncorrected $p < 0.001$ at voxel-level and FWE-corrected $p < 0.05$ at the cluster level; Fig. 5A). By contrast, linear increments in preparation-related activity were observed in the right M1, S1, and SMA. A linear increase in preparatory activity was also noted in fronto-parietal regions, including the bilateral inferior parietal lobule (IPL), middle frontal gyrus (MFG), bilateral superior temporal gyrus (STG), Thal, CB lobules, anterior cingulate cortex (ACC), and middle cingulate cortex (MCC) (FWE-corrected $p < 0.05$ at the cluster level; Fig. 5B).

Resting-state functional connectivity

The learning-related network, depicted as linear increments in preparation-related activity using task fMRI, overlapped with the FPN and SMN templates provided by the CONN toolbox (Fig. 6B). The relationships between Glu/GABA changes within M1 and resting-state M1 seed-based functional connectivity changes in the SMN and FPN after learning were investigated. A positive correlation was observed between changes in the Glu/GABA ratio and M1 seed-based resting-state functional connectivity changes in the FPN ($r_{(25)} = 0.48, p = 0.016$); no correlation was observed in the SMN ($r_{(25)} = -0.16$, $p = 0.435$) (Fig. 6C). The correlation between the FPN and changes in the Glu/GABA ratio was more prominent in parietal regions than in frontal regions (lateral prefrontal cortex [LPFC], $r_{(25)} = 0.35, p = 0.087$; posterior parietal cortex [PPC], $r_{(25)} = 0.58, p = 0.002$) (Fig. 7).

Sequence non-specific learning effect in the Control group

As shown in Figure 8, the control group did not show significant change in GABA/tCr concentration ($F_{(2,24)} = 0.275$; $p = 0.762$) and Glu/tCr concentration ($F_{(2,24)} = 3.014$; $p = 0.068$) in the right M1.

As shown in Figure 9A, the transition times in non-specific learning were 466.960 ± 97.564 for block 1, 409.301 ± 77.179 for block 2, 403.520 ± 64.868 for block 3, 400.546 ± 66.247 for block 4, and 393.746 ± 64.553 for block 5 (mean ± SD). Although repeated-measures ANOVA revealed a significant main effect of time (blocks 1–5) ($F_{(4,48)} = 21.064$; $p = 4.443\times10^{-10}$), no significant difference observed between block 5 and other blocks except for block 1 ($p = 0.001$ with Bonferroni correction). Approximately 10-20% performance improvement was observed. No significant correlation was observed between the change in the Glu/GABA ratio and performance improvement ($r_{(13)} = -0.09$, $p = 0.773$) in non-specific learning (Fig. 9B).

In non-specific learning no significant effect was observed in the linear increment in preparation-related activity in right M1 (T-score = 1.91, un-corrected $p = 0.080$).

No significant correlation was observed between changes in the Glu/GABA ratio and M1 seed-based resting-state functional connectivity changes in the FPN ($r_{(13)} = -0.32$, $p = 0.291$) and SMN ($r_{(13)} = 0.15$, $p = 0.616$) after non-specific learning (Fig. 10).

3.4 Discussion

Herein, we combined MRS, task fMRI, and resting-state fMRI to assess network level changes during motor sequence learning using a 7T MR machine. This study replicated and extended previous findings regarding the crucial role of M1 in motor sequence learning. To the best of our knowledge, this is the first report to demonstrate that the local excitatory-inhibitory balance within M1 regulates M1 connectivity with the FPN.

Advantage of 7T MRS over 3T MRS

GABA and Glu measurements were of high quality and reproducibility (Table 1). Although the neural excitatory-inhibitory balance is crucial for learning and memory, the main focus of prior studies on motor learning has been limited to the evaluation of GABA (Floyer-Lea et al., 2006; Stagg et al., 2011a, 2014; Sampaio-Baptista et al., 2015; King et al., 2020) due to technical limitations. The subtraction of two independent spectra to remove the overlap of signals is required in 3T MRS. Conversely, 7T MRS is able to concurrently resolve GABA, Glu, and glutamine (Gln), as sensitivity and chemical shift dispersion increase with increasing magnetic field strength (Tkáč et al., 2009). A higher SNR that increases linearly with the magnetic field strength enables a more accurate detection of weak signals from neurotransmitters in smaller voxels and with shorter measurement times (Terpstra et al., 2016). Neurotransmitters were measured within M1 using a voxel size of 8 cm^3 (2×2×2) at 7T in this study; however, a voxel size of 27 cm^3 (3×3×3) was selected at 3T (Greenhouse et al., 2017;

Sanaei-Nezhad et al., 2020). The 3T MRS is relatively insensitive to subtle changes in neurotransmitters underscoring cognitive functions due to large MRS voxel sizes (Talsma et al., 2019). Thus, 7T MRS has an advantage over 3T MRS for observing neurotransmitter function in a specifically localized brain region related to alterations in cognitive and behavioral task performance.

Learning-related changes in neurochemical metabolites within M1

We found significant reductions in Glu ($p < 0.05$, repeated-measures ANOVA and t-test with Bonferroni correction) between pre-task and post-task and between during-task and post-task (Fig. 2B). The decrease in Glu probably reflect the decrease in synaptic Glu or glutamatergic cycling as a part of energy metabolism in in the tricarboxylic acid (TCA) cycle (Ramadan et al., 2013). These findings indicate the learning-related decrease in Glu within M1 in motor sequence learning. One previous study using 7T machine showed no change in Glu within M1 during motor sequence learning using serial reaction time task (Kolasinski et al., 2019). Note should be made that, instead of implicit learning which mainly involved in the M1 (Honda et al. 1998), we adopted the explicit motor sequence learning which is known to recruit global brain network (Hamano et al., 2020; Sugawara et al., 2018). The motor engram was shown to be generated in the parietal regions distant from M1 during the explicit learning with the instruction of "tap the sequence as fast and correct as possible" (maximum mode), whereas generated in the M1 and dorsal premotor cortex during the implicit learning through visually guided constant speed execution (constant mode) (Hamano et al., 2020). Glu is known to exhibit a global effect on the BOLD response via glutamatergic projections to other cortical regions rather than modulating the BOLD response within the acquired MRS voxel (Falkenberg et al., 2012; Duncan et al., 2014). From these findings, the decrease in Glu is probably related to sequence learning-specific recruitment of the global brain network.

In terms of GABA, although previous studies showed GABA reduction in M1 during motor learning (Floyer-Lea et al., 2006; Kolasinski et al., 2019), no significant difference in GABA (Fig. 2B). Our results are in line with the recent study using similar motor sequential tasks (King et al., 2020). The GABA measured using the MRS thought to reflect bulk GABA from a large volume of interest, and is thought to predominantly reflect cellular, rather than synaptic GABA levels (Rae, 2014; Stagg et al., 2014). No correlation was observed between GABA with MRS and phasic GABA signaling using TMS (Stagg et al., 2011b, Dyke et al., 2017). Although a significant correlation between GABA with MRS and tonic GABA was observed in one study (Stagg et al., 2011b), no correlation was observed in a recent study (Dyke et al., 2017). The main factor of this difference in the two studies could be measurement methods of MRS: scan sequence (SPECIAL vs. STEAM) and magnetic field strength of the MR system (3T vs. 7T). That is, it seems to be that no consensus with the relationship between the GABA with MRS and tonic GABA.

We also measured GABA and Glu levels within M1 at pre-training and post-training resting-state conditions, and during task execution using a 7T MR system. We found the GABA change was significantly correlated with the performance improvement (*p* = 0.018), consistent with the previous finding (King et al., 2020). The disinhibition is to enhance Glu related excitatory processes resulting in decline of Glu concentration. The M1 comprises the intrinsic horizontal connection network necessary to support circuit reorganization during learning dependent on the precise balance of excitatory and inhibitory signaling within the M1 networks (Sanes and Donoghue, 2000). We adopted the Glu/GABA ratio to account for behavioral performance changes, as the stability of cortical areas during learning depends on the balance between cortical excitation and inhibition (Shibata et al., 2017). Further, considering that Glu is the precursor of GABA, their concentrations are likely to be reciprocally dependent. These factors indicate that the Glu/GABA ratio corresponds to cortical excitability (Dyke et al., 2017) and is a more sensitive proxy for plasticity than Glu or GABA alone. We observed a positive correlation between changes in the Glu/GABA ratio and task performance improvement (Fig. 3B). This finding suggests that between-participant variation in the balance of GABA and Glu reflects improvements in motor sequence learning performance.

Learning-related changes in preparatory BOLD activity including in M1

We observed that preparation-related activity increased linearly in fronto-parietal regions, especially in the right M1 (Fig. 5B). This result is consistent with that of our previous study (Hamano et al., 2019). In explicit motor sequence learning, participants needed to retrieve whole-sequence information at the preparation phases internally. Electrophysiological studies in nonhuman primates demonstrated an increase in neuronal responses reflecting preparatory activity for movement in M1 as learning progressed (Paz et al., 2003). Thus, the increase in preparation-related activity represents motor learning as an ecphoric process without being confounded by motor execution effects dependent on speed (Sadato et al., 1996, 1997; Jäncke et al., 1998) and force (Dettmers et al., 1995). The motor learning-related information of the specific sequence was accumulated in M1 because no such significant effect was observed in the M1 of the control group who conducted the sequential finger tapping with 120 different sequences. Additionally, an increment of the preparatory activity was highly present in regions included SMN and FPN, which suggests that the learning-related information is distributed in networks associated with both motor and executive controls.

Learning-related changes in M1-seeded functional connectivity with FPN

We also assessed resting-state M1 seed-based functional change elicited by motor sequence learning. As shown in Figure 6C, a positive correlation was observed between changes in the Glu/GABA ratio within M1 and M1 seed-based resting-state functional connectivity changes in FPN. By contrast, no correlation was noted in the SMN. Those results reflect the learning effect during motor sequence learning because no such correlation was observed in the control group (Fig. 10). The FPN controls coordinated behavior in a rapid, accurate, and flexible goal-driven manner (Marek and Dosenbach, 2018). Therefore, this finding indicates that motor learning driven by cognitive control is associated with local changes in excitatory-inhibitory balance in the M1. As described above, these findings reflect individual differences in skills, effort, and concentration of self-paced movement because participants were required to execute the task as quickly as possible during learning.

To further investigate the relationship between M1 and FPN, we assessed the correlations of connectivity changes in the bilateral PFC and PPC with changes in the Glu/GABA ratio within M1. These correlations were more prominent in parietal regions than in frontal regions, suggesting that the Glu/GABA ratio within M1 is more likely to affect the the connectivity with the PPC in FPN (Fig. 7). This finding concurs with the notion that the PPC is necessary for early and late learning phases, whereas the PFC is primarily involved in early learning phases (Dahms et al., 2020). The PFC processes sensory inputs, motor outputs, and working memory (Miller, 2000; Miller and Cohen, 2001; Halsband and Lange, 2006). The PPC, encompassing the IPL and SPL, processes spatial-sequential components (Jenkins et al., 1994; Honda et al., 1998). Both the M1 and PPC are critical hubs for the late motor sequence learning phase because these areas contribute to the delayed recall of learned motor sequences (Penhune and Doyon, 2002; Doyon et al., 2003). That is, in the later phase of learning, PPC and M1 are involved in retrieving the learned sequences acquired during the early learning phase. Our results, combined with our previous data, suggest that M1 integrates the accumulated information processed by the PPC in motor sequence learning.

The present finding is consistent with that of Sami et al. (2014), who investigated the consolidation effects on the resting state network using dual regression ICA analysis following an implicit and explicit learning, with serial reaction time, task. The authors had demonstrated the role of FPN in the explicit learning group, six hours following the initial acquisition, and have interpreted this finding as bringing the learnt sequence back to declarative awareness. Furthermore, they directly compared explicit and implicit groups at this late state, thereby identifying bilateral activation in both the parietal and premotor regions. The authors also speculated that this network might represent an engram of the extra procedural learning skill that had developed in the explicit acquisition group (Sami et al. 2014). Therefore, we conclude that the M1 centered network with FPN represents the formation of declarative procedural skill.

Constant BOLD response during execution and preparation phases

As shown in Figure 4, we observed similar spatial patterns of activity in the execution and preparation phases. These areas represent the large-scale functional motor network, necessary for performing sequential motor tasks. The selection of a particular motor sequence is based on inputs from the prefrontal cortex and parietal-temporal regions to the ventral premotor cortex (PMv) (Fagg and Arbib, 1998; Rizzolatti and Luppino, 2001). The dorsal part of the IPL (dIPL) is a multimodal sensory association region involved in the initial acquisition and learning of a motor task. The anterior parts of the IPL, PMv, and M1 comprise the fine motor control network (Rizzolatti and Luppino, 2001; Rizzolatti and Wolpert, 2005; Karabanov et al., 2012; Merchant et al., 2020). The dorsal premotor cortex (PMd) is involved in movement selection (Grafton et al., 1998). Additionally, preparation-related activity was most prominently associated with enhanced activity in the putamen (Fig. 4B), suggesting that this preparatory activity represents preceding self-initiated movements (Schultz and Romo, 1992). Our findings are consistent with previous results demonstrating preparatory activity in the motor, somatosensory, parietal, and prefrontal cortical regions; basal ganglia; and cerebellum in sequential finger movements (Nambu et al., 2015).

Limitations

The participants recruited in this study were predominantly women, with bodyweights of 60 kg or less. This limitation contributed to technical challenges in MRS measurements using a single-transmit 7T MR system. First, the B1 transmit field inhomogeneity was enhanced. The suppression of water signals for the measurement of metabolites may have been insufficient depending on the head size, and it was challenging to obtain good spectral quality. Second, adjustments of MRS sequence parameters may have been necessary, involving a lengthening of measurement time to solve the local specific absorption rate limitations partly defined using body weight. Gender differences are known to effect visuo-motor adaptation learning of throwing (Moreno-Briseño et al., 2010); given that the participants in this study were primarily women, the generalizability of the results remain limited, and further studies are warranted, where the number of men is high or at least equivalent to that of women.

Conclusion

In conclusion, our findings indicate that motor learning driven by cognitive control is associated with local variation in the excitatory-inhibitory balance in M1 that regulates remote connectivity with the FPN, constituting the M1-centered motor learning network.

3.5 References

Allen M, Poggiali D, Whitaker K, Marshall TR, Kievit RA (2019) Raincloud plots: a multi-platform tool for robust data visualization. Wellcome Open Res 4:63.

Andersson JLR, Skare S, Ashburner J (2003) How to correct susceptibility distortions in spin-echo echo-planar images: Application to diffusion tensor imaging. Neuroimage 20:870–888.

Behzadi Y, Restom K, Liau J, Liu TT (2007) A component based noise correction method (CompCor) for BOLD and perfusion based fMRI. Neuroimage 37:90–101.

Chenji S, Jha S, Lee D, Brown M, Seres P, Mah D, Kalra S (2016) Investigating default mode and sensorimotor network connectivity in amyotrophic lateral sclerosis. PLoS One 11:1–14.

Cox RW (1996) AFNI: Software for analysis and visualization of functional magnetic resonance neuroimages. Comput Biomed Res 29:162–173.

Dahms C, Brodoehl S, Witte OW, Klingner CM (2020) The importance of different learning stages for motor sequence learning after stroke. Hum Brain Mapp 41:270–286.

Dayan E, Cohen LG (2011) Neuroplasticity subserving motor skill learning. Neuron 72:443–454.

Debas K, Carrier J, Orban P, Barakat M, Lungu O, Vandewalle G, Tahar AH, Bellec P, Karni A, Ungerleider LG, Benali H, Doyon J (2010) Brain plasticity related to the consolidation of motor sequence learning and motor adaptation. Proc Natl Acad Sci U S A 107:17839–

17844.

Dettmers C, Fink GR, Lemon RN, Stephan KM, Passingham RE, Silbersweig D, Holmes A, Ridding MC, Brooks DJ, Frackowiak RS (1995) Relation between cerebral activity and force in the motor areas of the human brain. J Neurophysiol 74:802–815.

Doyon J, Penhune V, Ungerleider LG (2003) Distinct contribution of the cortico-striatal and cortico-cerebellar systems to motor skill learning. Neuropsychologia 41:252–262.

Dupont-Hadwen J, Bestmann S, Stagg CJ (2019) Motor training modulates intracortical inhibitory dynamics in motor cortex during movement preparation. Brain Stimul 12:300–308.

Duncan NW, Wiebking C, Northoff G (2014) Associations of regional GABA and glutamate with intrinsic and extrinsic neural activity in humans-A review of multimodal imaging studies. Neurosci Biobehav Rev 47:36–52.

Dyke K, Pépés SE, Chen C, Kim S, Sigurdsson HP, Draper A, Husain M, Nachev P, Gowland PA, Morris PG, Jackson SR (2017) Comparing GABA-dependent physiological measures of inhibition with proton magnetic resonance spectroscopy measurement of GABA using ultra-high-field MRI. Neuroimage 152:360–370.

Fagg AH, Arbib MA (1998) Modeling parietal-premotor interactions in primate control of grasping. Neural Networks 11:1277–1303.

Falkenberg LE, Westerhausen R, Specht K, Hugdahl K (2012) Resting-state glutamate level in the anterior cingulate predicts blood-oxygen level-dependent response to cognitive control.

Proc Natl Acad Sci U S A 109:5069–5073.

Fischer S, Hallschmid M, Elsner AL, Born J (2002) Sleep forms memory for finger skills. Proc Natl Acad Sci U S A 99:11987–11991.

Fischer S, Nitschke MF, Melchert UH, Erdmann C, Born J (2005) Motor memory consolidation in sleep shapes more effective neuronal representations. J Neurosci 25:11248–11255.

Floyer-Lea A, Wylezinska M, Kincses T, Matthews PM (2006) Rapid modulation of GABA concentration in human sensorimotor cortex during motor learning. J Neurophysiol 95:1639–1644.

Friston KJ, Jezzard P, Turner R (1994) Analysis of functional MRI time-series. Hum Brain Mapp 1:153–171.

Friston KJ, Holmes A, Poline JB., Price CJ, Frith CD (1996) Detecting activations in pet and fMRI: Levels of inference and power. Neuroimage 4:223–235.

Friston KJ, Glaser DE, Henson RNA, Kiebel S, Phillips C, Ashburner J (2002) Classical and Bayesian inference in neuroimaging: Applications. Neuroimage 16:484–512.

Glasser MF, Sotiropoulos SN, Wilson JA, Coalson TS, Fischl B, Andersson JL, Xu J, Jbabdi S, Webster M, Polimeni JR, Van Essen DC, Jenkinson M (2013) The minimal preprocessing pipelines for the Human Connectome Project. Neuroimage 80:105–124.

Grafton ST, Fagg AH, Arbib MA (1998) Dorsal premotor cortex and conditional movement selection: A PET functional mapping study. J Neurophysiol 79:1092–1097.

Greenhouse I, King M, Noah S, Maddock RJ, Ivry RB (2017) Individual Differences in Resting

Corticospinal Excitability Are Correlated with Reaction Time and GABA Content in Motor Cortex. J Neurosci 37:2686–2696.

Griswold MA, Jakob PM, Heidemann RM, Nittka M, Jellus V, Wang J, Kiefer B, Haase A (2002) Generalized autocalibrating partially parallel acquisitions (GRAPPA). Magn Reson Med 47:1202–1210.

Gruetter R (1993) Automatic, localized in vivo adjustment of all first- and second-order shim coils. Magn Reson Med 29:804–811.

Gruetter R, Tkáč I (2000) Field mapping without reference scan using asymmetric echo-planar techniques. Magn Reson Med 43:319–323.

Guadagnoli MA, Lee TD (2004) Challenge point: a framework for conceptualizing the effects of various practice conditions in motor learning. J Mot Behav 36:212–224.

Halsband U, Lange RK (2006) Motor learning in man: A review of functional and clinical studies. J Physiol 99:414–424.

Hamano YH, Sugawara SK, Fukunaga M, Sadato N (2019) The integrative role of the M1 for the motor sequence learning. Program No. 311.13. 2019 Neuroscience Meeting Planner. Chicago, IL: Society for Neuroscience, 2019.

Hamano YH, Sugawara SK, Yoshimoto T, Sadato N (2020) The motor engram as a dynamic change of the cortical network during early sequence learning: An fMRI study. Neurosci Res 153:27–39.

Holmes AP, Friston KJ (1998) Generalisability, random effects & population inference.

Neuroimage 7:S754.

Honda M, Deiber M-P, Ibáñez V, Pascual-Leone A, Zhuang P, Hallett M (1998) Dynamic cortical involvement in implicit and explicit motor sequence learning. A PET study. Brain 121:2159–2173.

Jäncke L, Peters M, Schlaug G, Posse S, Steinmetz H, Müller-Gärtner H (1998) Differential magnetic resonance signal change in human sensorimotor cortex to finger movements of different rate of the dominant and subdominant hand. Brain Res Cogn Brain Res 6:279–284.

Jenkins IH, Brooks DJ, Nixon PD, Frackowiak RSJ, Passingham RE (1994) Motor sequence learning: A study with positron emission tomography. J Neurosci 14:3775–3790.

Karabanov A, Jin SH, Joutsen A, Poston B, Aizen J, Ellenstein A, Hallett M (2012) Timing-dependent modulation of the posterior parietal cortex-primary motor cortex pathway by sensorimotor training. J Neurophysiol 107:3190–3199.

King BR, Rumpf JJ, Verbaanderd E, Heise KF, Dolfen N, Sunaert S, Doyon J, Classen J, Mantini D, Puts NAJ, Edden RAE, Albouy G, Swinnen SP (2020) Baseline sensorimotor GABA levels shape neuroplastic processes induced by motor learning in older adults. Hum Brain Mapp 41:3680–3695.

Klose U (1990) In vivo proton spectroscopy in presence of eddy currents. Magn Reson Med 14:26–30.

Kolasinski J, Hinson EL, Divanbeighi Zand AP, Rizov A, Emir UE, Stagg CJ (2019) The dynamics of cortical GABA in human motor learning. J Physiol 597:271–282.

Marek S, Dosenbach NUF (2018) The frontoparietal network: function, electrophysiology, and importance of individual precision mapping. Dialogues Clin Neurosci 20:133–140.

Marjańska M, Terpstra M (2019) Influence of fitting approaches in LCModel on MRS quantification focusing on age-specific macromolecules and the spline baseline. NMR Biomed:e4197.

Merchant SHI, Frangos E, Parker J, Bradson M, Wu T, Vial-Undurraga F, Leodori G, Bushnell MC, Horovitz SG, Hallett M, Popa T (2020) The role of the inferior parietal lobule in writer's cramp. Brain 143:1766–1779.

Miller GA, Galanter E, Pribram KH (1960) Plans and the structure of behavior (Holt, Rinehart and Winston, New York).

Miller EK (2000) The prefrontal cortex and cognitive control. Nat Rev Neurosci 1:59–65.

Miller EK, Cohen JD (2001) An integrative theory of prefrontal cortex function. Annu Rev Neurosci 24:167–202.

Moeller S, Yacoub E, Olman CA, Auerbach E, Strupp J, Harel N, Uğurbil K (2010) Multiband multislice GE-EPI at 7 tesla, with 16-fold acceleration using partial parallel imaging with application to high spatial and temporal whole-brain FMRI. Magn Reson Med 63:1144–1153.

Moreno-Briseño P, Díaz R, Campos-Romo A, Fernandez-Ruiz J (2010) Sex-related differences in motor learning and performance. Behav Brain Funct 6:74.

Mugler JP (2014) Optimized three-dimensional fast-spin-echo MRI. J Magn Reson Imaging 39:745–767.

Mugler JP, Brookeman JR (1990) Three-dimensional magnetization-prepared rapid gradient-echo imaging (3D MP RAGE). Magn Reson Med 15:152–157.

Nambu I, Hagura N, Hirose S, Wada Y, Kawato M, Naito E (2015) Decoding sequential finger movements from preparatory activity in higher-order motor regions: A functional magnetic resonance imaging multi-voxel pattern analysis. Eur J Neurosci 42:2851–2859.

Oldfield RCC (1971) The assessment and analysis of handedness: The Edinburgh inventory. Neuropsychologia 9:97–113.

Paz R, Boraud T, Natan C, Bergman H, Vaadia E (2003) Preparatory activity in motor cortex reflects learning of local visuomotor skills. Nat Neurosci 6:882–890.

Penhune VB, Doyon J (2002) Dynamic cortical and subcortical networks in learning and delayed recall of timed motor sequences. J Neurosci 22:1397–1406.

Provencher SW (1993) Estimation of metabolite concentrations from localized in vivo proton NMR spectra. Magn Reson Med 30:672–679.

Provencher SW (2001) Automatic quantitation of localized in vivo 1H spectra with LCModel. NMR Biomed 14:260–264.

Rae CD (2014) A guide to the metabolic pathways and function of metabolites observed in human brain 1H magnetic resonance spectra. Neurochem Res 39:1–36.

Ramadan S, Lin A, Stanwell P (2013) Glutamate and glutamine: A review of in vivo MRS in the human brain. NMR Biomed 26:1630–1646.

Riedel G, Platt B, Micheau J (2003) Glutamate receptor function in learning and memory. Behav Brain Res 140:1–47.

Rizzolatti G, Luppino G (2001) The cortical motor system. Neuron 31:889–901.

Rizzolatti G, Wolpert DM (2005) Motor systems. Curr Opin Neurobiol 15:623–625.

Sadato N, Ibañez V, Deiber MP, Campbell G, Leonardo M, Hallett M (1996) Frequency-dependent changes of regional cerebral blood flow during finger movements. J Cereb Blood Flow Metab 16:23–33.

Sadato N, Ibañez V, Campbell G, Deiber MP, Le Bihan D, Hallett M (1997) Frequency-dependent changes of regional cerebral blood flow during finger movements: Functional MRI compared to pet. J Cereb Blood Flow Metab 17:670–679.

Sami S, Robertson EM, Miall RC (2014) The time course of task-specific memory consolidation effects in resting state networks. J Neurosci 34:3982–3992.

Sampaio-Baptista C, Filippini N, Stagg CJ, Near J, Scholz J, Johansen-Berg H (2015) Changes in functional connectivity and GABA levels with long-term motor learning. Neuroimage 106:15–20.

Sanaei-Nezhad F, Lea-Carnall CA, Anton A, Jung JY, Michou E, Williams SR, Parkes LM (2020) Number of subjects required in common study designs for functional GABA magnetic resonance spectroscopy in the human brain at 3 Tesla. Eur J Neurosci 51:1784–1793.

Sanes JN, Donoghue JP (2000) Plasticity and primary motor cortex. Annu Rev Neurosci 23:393–415.

Schultz W, Romo R (1992) Role of primate basal ganglia and frontal cortex in the internal generation of movements - I. Preparatory activity in the anterior striatum. Exp Brain Res 91:363–384.

Shibata K, Sasaki Y, Bang JW, Walsh EG, Machizawa MG, Tamaki M, Chang LH, Watanabe T (2017) Overlearning hyperstabilizes a skill by rapidly making neurochemical processing inhibitory-dominant. Nat Neurosci 20:470–475.

Shmuelof L, Krakauer JW (2011) Are we ready for a natural history of motor learning? Neuron 72:469–476.

Shmuelof L, Krakauer JW, Mazzoni P (2012) How is a motor skill learned? Change and invariance at the levels of task success and trajectory control. J Neurophysiol 108:578–594.

Simpson R, Devenyi GA, Jezzard P, Hennessy TJ, Near J (2017) Advanced processing and simulation of MRS data using the FID appliance (FID-A)—An open source, MATLAB-based toolkit. Magn Reson Med 77:23–33.

Stagg CJ, Bachtiar V, Johansen-Berg H (2011a) The role of GABA in human motor learning. Curr Biol 21:480–484.

Stagg CJ, Bestmann S, Constantinescu AO, Moreno Moreno L, Allman C, Mekle R, Woolrich M, Near J, Johansen-Berg H, Rothwell JC (2011b) Relationship between physiological measures of excitability and levels of glutamate and GABA in the human motor cortex. J Physiol 589:5845–5855.

Stagg CJ, Bachtiar V, Amadi U, Gudberg CA, Ilie AS, Sampaio-Baptista C, O'Shea J, Woolrich M, Smith SM, Filippini N, Near J, Johansen-Berg H (2014) Local GABA concentration is related to network-level resting functional connectivity. eLife 3:e01465.

Steele PM, Mauk MD (1999) Inhibitory control of LTP and LTD: Stability of synapse strength. J Neurophysiol 81:1559–1566.

Sugawara SK, Masaki F, Hamano YH, Yoshimoto T, Sadato N (2018) Motor engram is encoded in dormant neuronal network. 11th Forum of the Federation of European Neuroscience Societies (FENS), Berlin, Germany. 7-11 July 2018. FENS Abstract F004.

Talsma L, Loon A van, Scholte HS, Slagter H (2019) State or trait? MRS-measured GABA and glutamate concentrations are not modulated by task demand and do not robustly predict task performance. bioRxiv 543140. doi: 10.1101/543140.

Teeuwisse WM, Brink WM, Haines KN, Webb AG (2012a) Simulations of high permittivity materials for 7 T neuroimaging and evaluation of a new barium titanate-based dielectric. Magn Reson Med 67:912–918.

Teeuwisse WM, Brink WM, Webb AG (2012b) Quantitative assessment of the effects of high-permittivity pads in 7 Tesla MRI of the brain. Magn Reson Med 67:1285–1293.

Terpstra M, Cheong I, Lyu T, Deelchand DK, Emir UE, Bednařík P, Eberly LE, Öz G (2016) Test-retest reproducibility of neurochemical profiles with short-echo, single-voxel MR spectroscopy at 3T and 7T. Magn Reson Med 76:1083–1091.

Tkáč I, Starčuk Z, Choi IY, Gruetter R (1999) In vivo 1H NMR spectroscopy of rat brain at 1 ms echo time. Magn Reson Med 41:649–656.

Tkáč I, Öz G, Adriany G, Uğurbil K, Gruetter R (2009) In vivo 1H NMR spectroscopy of the human brain at high magnetic fields: Metabolite quantification at 4T vs. 7T. Magn Reson Med 62:868–879.

Tzourio-Mazoyer N, Landeau B, Papathanassiou D, Crivello F, Etard O, Delcroix N, Mazoyer B, Joliot M (2002) Automated anatomical labeling of activations in SPM using a macroscopic anatomical parcellation of the MNI MRI single-subject brain. Neuroimage 15:273–289.

Vincent JL, Kahn I, Snyder AZ, Raichle ME, Buckner RL (2008) Evidence for a frontoparietal control system revealed by intrinsic functional connectivity. J Neurophysiol 100:3328–3342.

Vu AT, Jamison K, Glasser MF, Smith SM, Coalson T, Moeller S, Auerbach EJ, Uğurbil K, Yacoub E (2017) Tradeoffs in pushing the spatial resolution of fMRI for the 7T Human Connectome Project. Neuroimage 154:23–32.

Wadden KP, Hodges NJ, De Asis KL, Neva JL, Boyd LA (2019) Individualized challenge point practice as a method to aid motor sequence learning. J Mot Behav 51:467–485.

Walker MP, Brakefield T, Morgan A, Hobson JA, Stickgold R (2002) Practice with sleep makes perfect: Sleep-dependent motor skill learning. Neuron 35:205–211.

Walker MP, Brakefield T, Hobson JA, Stickgold R (2003) Dissociable stages of human memory consolidation and reconsolidation. Nature 425:616–620.

Webb AG (2011) Dielectric materials in magnetic resonance. Concepts Magn Reson Part A 38A:148–184.

Whitfield-Gabrieli S, Nieto-Castanon A (2012) Conn: A functional connectivity toolbox for correlated and anticorrelated brain networks. Brain Connect 2:125–141.

Worsley KJ, Friston KJ (1995) Analysis of fMRI time-series revisited—again. Neuroimage 2:173–181.

Yamamoto T, Fukunaga M, Sugawara SK, Hamano YH, Sadato N (2020) Quantitative Evaluations of Geometrical Distortion Corrections in Cortical Surface-Based Analysis of High-Resolution Functional MRI Data at 7 Tesla. J Magn Reson Imaging, in-press. doi:10.1002/jmri.27420

3.6 Figure Legends

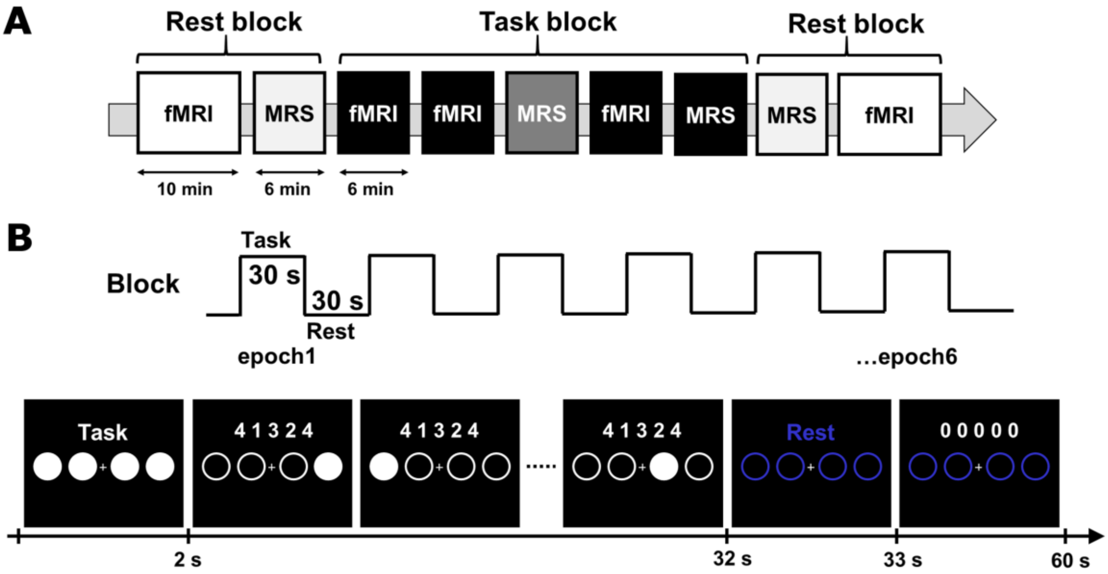

Figure 1. **Experimental design**

(A) The timeline of combined fMRI and MRS sessions. The experiment consisted of the pre-learning rest session, followed by the task and post-learning rest session. During the rest of the sessions, fMRI and MRS scans were conducted before and after motor sequence learning. During the task session, participants underwent four fMRI and one MRS scan with sequential finger-tapping learning tasks.

(B) Task design. Task blocks (1–5) consisted of six cycles of task and rest epochs. Prior to task execution, participants were instructed to retrieve and prepare for the motor sequences following the instructions and closed circles. Participants were presented with a five-digit sequence (e.g. “4-1-3-2-4”) for 30 s during the task epoch. During the rest epoch, four open blue circles were presented.

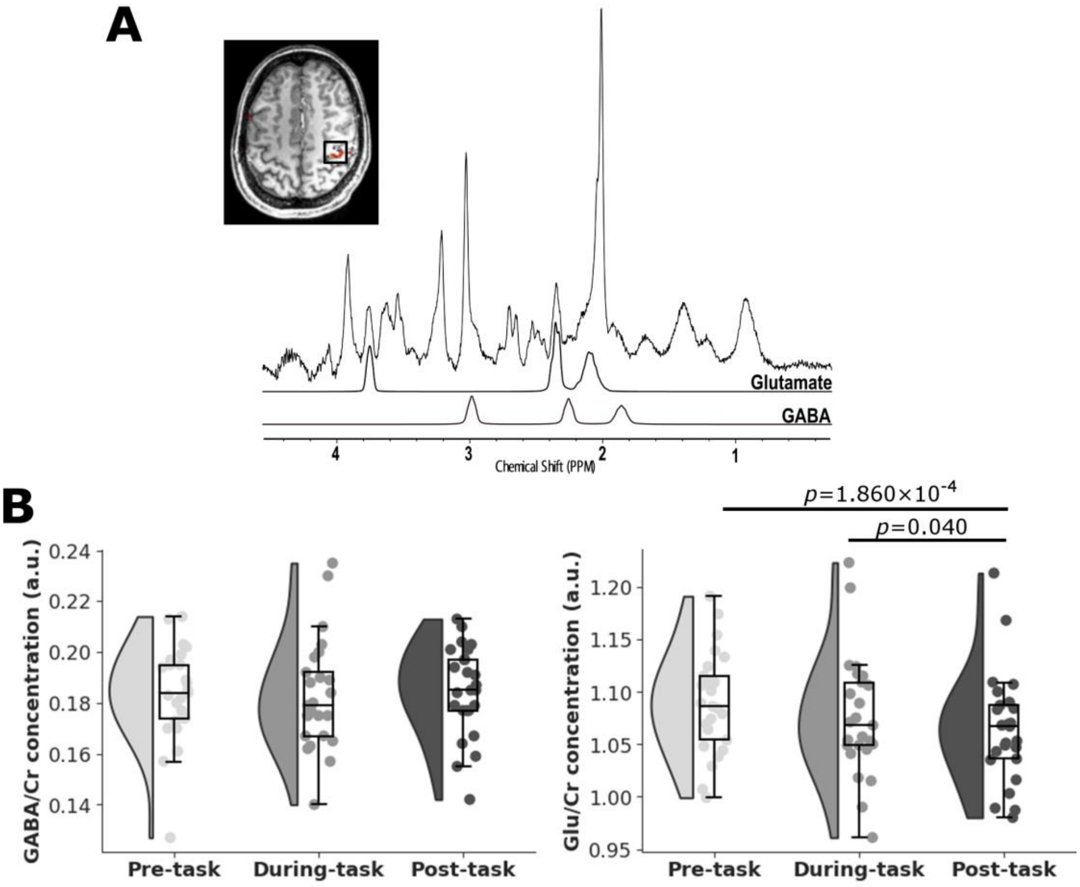

Figure 2. **MR spectra and neurotransmitter levels**

(A) The 2×2×2 cm^3 volume of interest (black square) was centered over the hand knob area of right M1 identified using fMRI during a finger opposition task (red) and was superimposed on the T1w MPRAGE image. (B) Violin plots coupled with boxplots showing the distribution of the concentrations of GABA and glutamate (Glu) during the pre-task (light gray), during-task (dark gray), and post-task (black) periods. Each dot represents a data point (n = 25). The boxplots represent the median and upper/lower quartiles of the data, and the vertical lines represent the highest/lowest values.

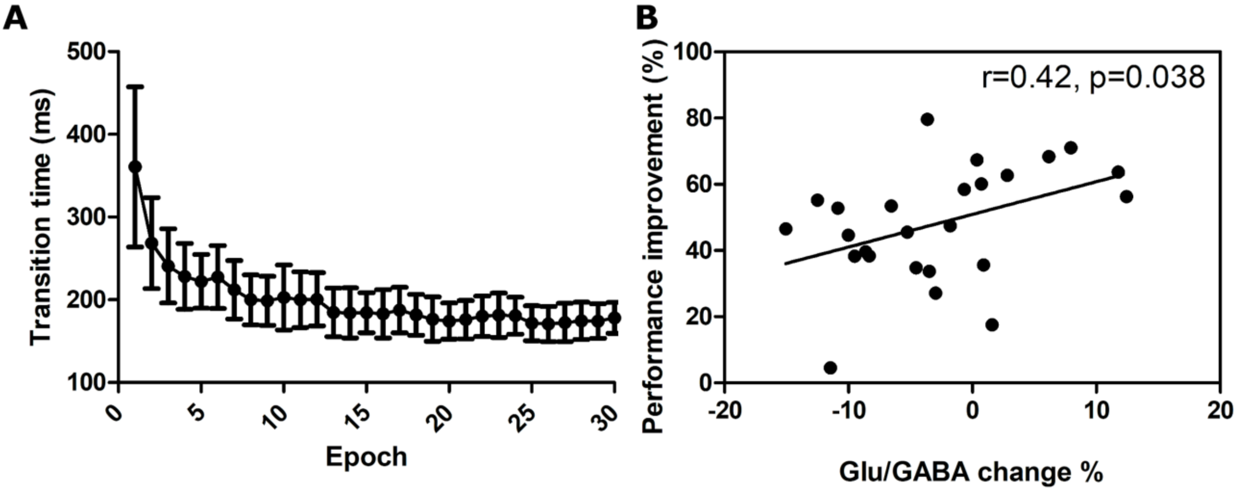

Figure 3. Changes in Glu/GABA ratio in relation to behavioral performance improvement

(A) Task performance in motor sequence learning. Task performance was measured using transition time, defined as the median time between two correct button responses per epoch. Data are presented as mean ± standard deviation (SD) for n = 25. (B) Relationship between Glu/GABA changes within right M1 and performance improvement.

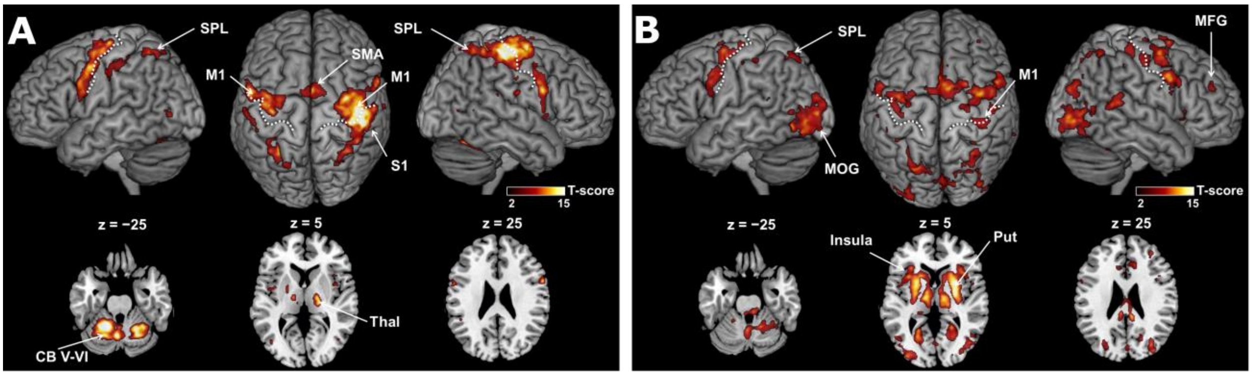

Figure 4. Constant changes during execution and preparation.

(A) Execution-related and (B) preparation-related activity superimposed on the surface-rendered high-resolution MRI of the template brain. The white dotted lines indicate the central sulcus. The level of statistical significance was set at $p < 0.05$, FWE-corrected for multiple comparisons at the voxel-level.

CB, cerebellum; SPL, superior parietal lobule; MFG, middle frontal gyrus; MOG, middle occipital gyrus; S1, primary somatosensory cortex; M1, primary motor cortex; Thal, thalamus; Put, putamen; SMA, supplementary motor area.

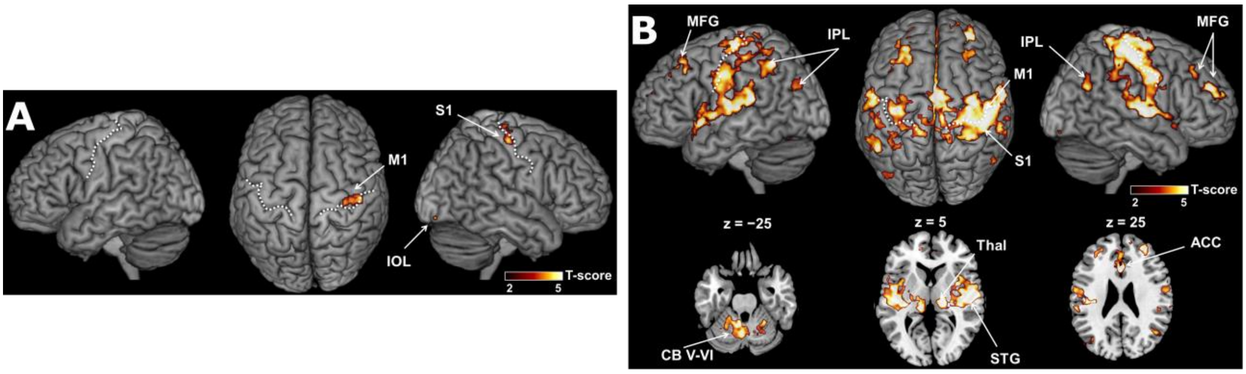

Figure 5. Learning related changes during execution and preparation.

Linear increments in (A) execution-related and (B) preparation-related activity superimposed on the surface-rendered high-resolution MRI of the template brain. The white dotted lines indicate the central sulcus. The level of statistical significance was set at $p < 0.05$, FWE-corrected for multiple comparisons at the cluster-level.

CB, cerebellum; IPL, inferior parietal lobule; MFG, middle frontal gyrus; S1, primary somatosensory cortex; M1, primary motor cortex; SMA, supplementary motor area; STG, superior temporal gyrus; Thal, thalamus; ACC, anterior cingulate cortex.

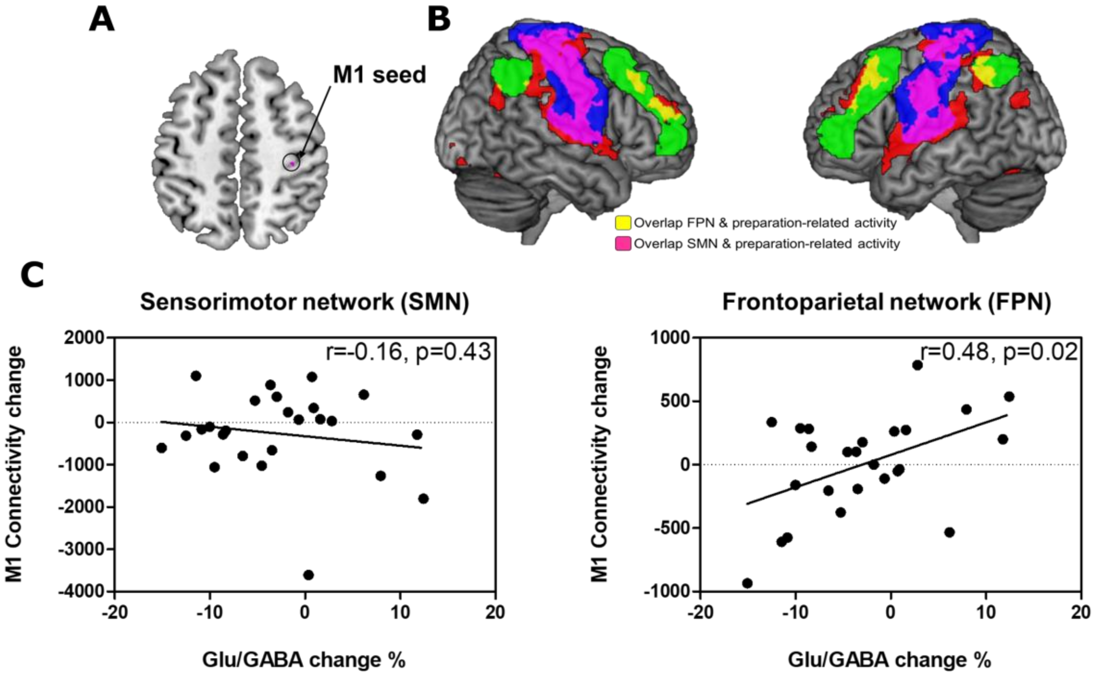

Figure 6. ROI-based analysis of functional connectivity between the right M1 and FPN or SMN

(A) M1 seed ROI depicted by the linear increments in preparation-related activity. The level of statistical significance was set at *p* < 0.05, FWE-corrected for multiple comparisons at the voxel-level. (B) ROI overlap of sensorimotor network (SMN: blue) and fronto-parietal network (FPN: green) with the learning-related network, depicted as the linear increments in preparation-related activity using task fMRI (red). SMN and FPN were defined based on the CONN toolbox. (C) Relationships between Glu/GABA changes within right M1 and M1 seed-based resting-state functional connectivity changes in the SMN and FPN after motor sequence learning. M1 seed-based resting-state functional connectivity changes were calculated from the sum of changes in connectivity values between pre-task and post-task periods in the networks.

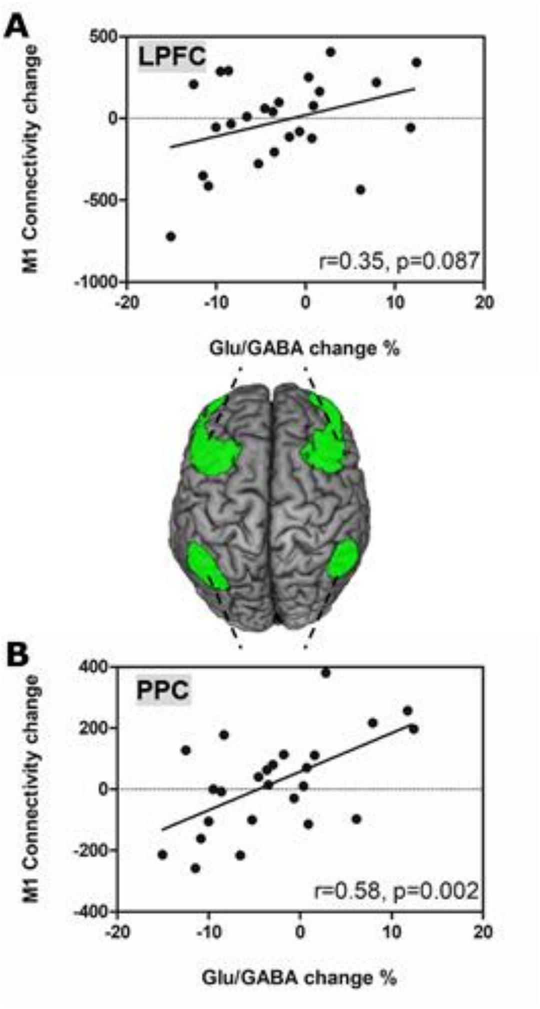

Figure 7. ROI-based analysis of functional connectivity between the right M1 and subregions of FPN

Relationships between the changes in Glu/GABA ratio within the right M1 and M1 seed-based resting-state functional connectivity changes in (A) lateral prefrontal cortex (LPFC) and (B) posterior parietal cortex (PPC) of the fronto-parietal network (FPN: green) after motor sequence learning.

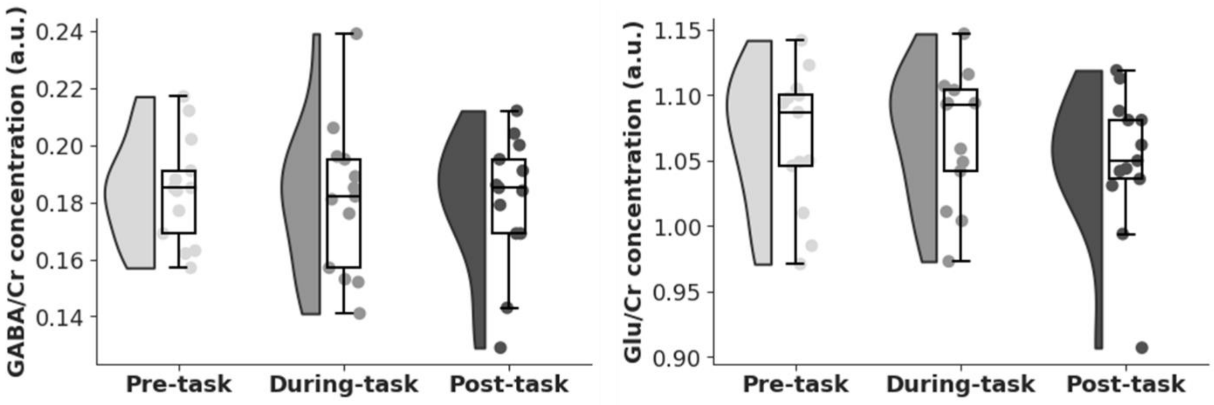

Figure 8. **Neurotransmitter levels change in non-specific learning**

Violin plots coupled with boxplots showing the distribution of the concentrations of GABA and glutamate (Glu) during the pre-task (light gray), during-task (dark gray), and post-task (black) periods in non-specific learning. Each dot represents a data point (n = 13). The boxplots represent the median and upper/lower quartiles of the data, and the vertical lines represent the highest/lowest values.

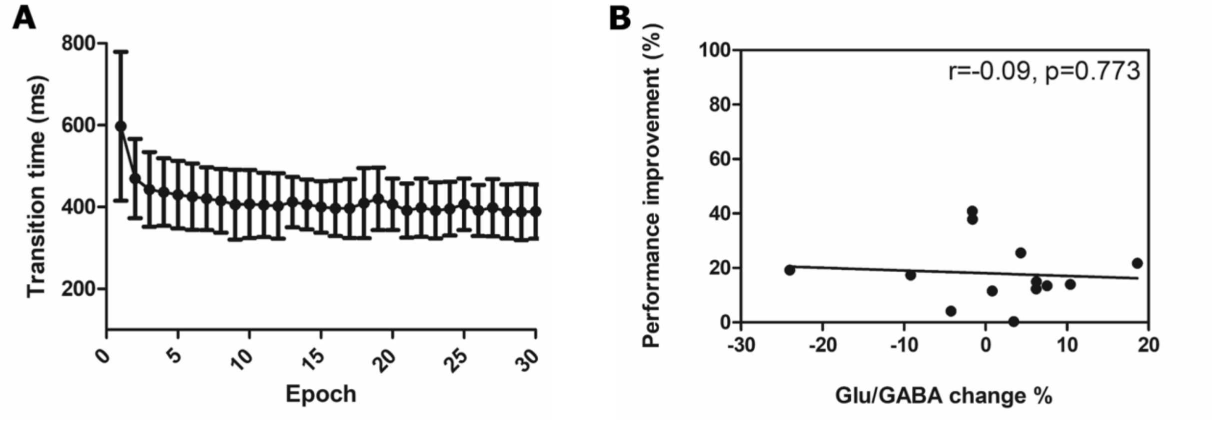

Figure 9. Changes in Glu/GABA ratio in relation to behavioral performance improvement in non-specific learning

(A) Task performance in non-specific motor sequence learning. Task performance is measured using transition time, defined as the median time between two correct button responses per epoch. Data are presented as mean ± standard deviation (SD) for n = 13. (B) Relationship between Glu/GABA changes within right primary motor cortex and performance improvement in non-specific learning.

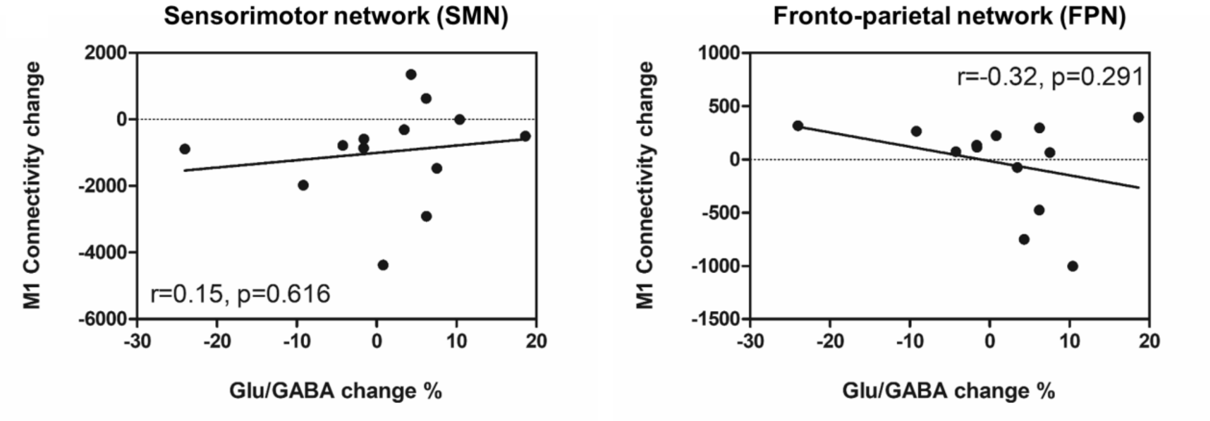

Figure 10. ROI-based analysis of functional connectivity between the right M1 and FPN or SMN in non-specific learning

Relationships between Glu/GABA changes within right M1 and M1 seed-based resting-state functional connectivity changes in the SMN and FPN after non-specific learning. M1 seed-based resting-state functional connectivity changes are calculated from the sum of changes in connectivity values between pre-task and post-task periods in the networks.

3.7 Tables

Table 1. MRS spectra quality of pre-task, during-task, and post-task periods

	CRLB (GABA)	CRLB (Glu)	CRLB (tCr)	Linewidth
Pre-task	9.7 ± 1.1	2.1 ± 0.2	1.9 ± 0.2	12.6 ± 1.1
During-task	9.5 ± 1.1	2.1 ± 0.3	1.9 ± 0.3	12.7 ± 1.3
Post-task	9.7 ± 1.0	2.2 ± 0.4	1.9 ± 0.3	12.8 ± 1.3
Main effect	$F[2,74]=0.984$	$F[2,74]=3.171$	$F[2,74]=0.196$	$F[2,74]=1.076$
of time	$p = 0.379$	$p = 0.059$	$p = 0.823$	$p = 0.346$

Data are presented as mean ± standard deviation (SD) for n = 38.

CRLB, Cramer–Rao lower bounds; Glu, glutamate; tCr, total creatine

4. Conclusion

I applied ultrahigh magnetic field 7T MR systems to structural and functional analysis of human brain. I successfully visualize the internal segments of GPi with high resolution and contrast within practical time for clinical application using a 7T MRI scanner in Study I. Also, I could develop an understanding about M1-centered network dynamics in sequential motor learning by combing the MRS and fMRI at 7T in Study II. These results demonstrated that 7T MR systems identified the anatomical information in the local region of the human brain and elucidated the dynamic mechanism behind brain network changes, which was difficult in terms of sensitivity and accuracy at conventional MR systems. It is expected to contribute to develop the understanding of the advance knowledge of brain anatomy and function.

5. Acknowledgements

I would like to show my deepest gratitude to my supervisor, Prof. Norihiro Sadato for his continued support and encouragement through the doctoral program. I am deeply indebted to Dr. Masaki Fukunaga for helping to make present studies possible and providing insightful comments and technical supports. Special thanks go to Dr. Sho Sugawara, Dr. Yuki Hamano and Dr. Tetsuya Yamamoto for helping to make stimulation programs and analyze the data in Study II. Also, I would like to thank Prof. Atsushi Nambu and Prof. Masaki Isoda for the mentorship as part of the doctoral course of Life Science Progress.

I would like to thank Dr. Małgorzata Marjańska, Dr. Edward J. Auerbach, Dr. Essa Yacoub, Dr. Steen Moeller (Center for Magnetic Resonance Research, University of Minnesota) for providing the MRS and fMRI sequences, and Dr. Hans Peter Fautz, Dr. Tobias Kober, Dr. Tim DeVito, and Dr. Josef Pfeuffer (Siemens Healthineers GmbH) for providing the sequences of pre-scanning adjustment on 7T MRI.

Finally, I would like to extend my gratitude to all laboratory members of Division of Cerebral Integration in NIPS. Their meticulous comments and gently supports to an enormous help to me.